Title
Superconducting Multilayer VIA

Permalink
https://escholarship.org/uc/item/5h11967x

Author
Ramakrishna, Sourabh

Publication Date
2023

UNIVERSITY OF CALIFORNIA
RIVERSIDE

Superconducting Multilayer VIA

A Thesis submitted in partial satisfaction
of the requirements for the degree of

Master of Science

in

Electrical Engineering

by

Sourabh Ramakrishna

June 2023

Dissertation Committee:

Dr. Shane A. Cybart, Chairperson
Dr. Roger Lake
Dr. Ming Liu

The Thesis of Sourabh Ramakrishna is approved:

Committee Chairperson

University of California, Riverside

Acknowledgments

I am deeply indebted to many individuals and organizations whose support and guidance have been invaluable in the completion of this Master Thesis.

First and foremost, I would like to express my sincere appreciation to my thesis supervisor, Dr. Shane Cybart, whose mentorship, insights, and encouragement have been instrumental in shaping this thesis. Their constructive feedback and expert guidance have challenged me to think critically and creatively, and have helped me refine my research questions and arguments.

I would also like to acknowledge the members of my thesis committee, Dr. Roger Lake and Dr. Ming Liu, for their thoughtful comments, suggestions, and questions, which have pushed me to explore new avenues of inquiry and to deepen my understanding of the research topic. Their feedback has been invaluable in shaping the structure and content of this thesis.

I am grateful to the faculty members of Department of Electrical and Computer Engineering, who have provided me with a rigorous and intellectually stimulating academic environment, as well as access to resources and facilities that have enabled me to conduct my research. I am also thankful to the staff members of University of California Riverside, who have provided administrative and technical support, and who have been available to assist me whenever needed.

I owe a debt of gratitude to my family and friends, who have provided me with unwavering support and encouragement throughout my academic journey. Their love, understanding, and patience have helped me persevere through the challenges and obstacles that I have encountered along the way.

Finally, I would like to express my heartfelt appreciation to the participants in my research, Dr. Nirjhar Sarkar (Post Doc), Dr. Ilkeun Lee (Scientist), Adhilsha Parachikunnumal, Joseph Forman, Sreekar Vattipalli, Alexander Brooks and Adam Miller (current PhD students) whose willingness to share their experiences, opinions, and insights has enriched my understanding of the research topic. Their contributions have been invaluable in shaping the analysis and findings of this thesis.

I would like to thank everyone who has supported me in the completion of this thesis. Your contributions have been essential in making this project a success.

I would like to extend my deepest gratitude to my parents amma appa, my sister Supritha, and my dearest friends for their unwavering love, support, and encouragement throughout my academic journey. I am forever grateful for their love and support.

This one's for you Amma.

ABSTRACT OF THE THESIS

Superconducting Multilayer VIA

by

Sourabh Ramakrishna

Master of Science, Graduate Program in Electrical Engineering
University of California, Riverside, June 2023
Dr. Shane A. Cybart, Chairperson

Multilayer vias play a crucial role in the interconnection of different layers within electronic devices, enabling the transmission of signals and facilitating complex circuit designs. This abstract presents a comprehensive overview of the structural analysis and fabrication approach for multilayer vias, focusing on their importance, fabrication techniques, and characterization methods.

The abstract emphasizes the significance of multilayer vias as key components in modern electronic devices, enabling efficient signal transmission and improving overall circuit performance. It highlights the importance of understanding the structural properties of these vias to ensure their functionality and reliability.

The abstract also discusses various fabrication techniques employed for multilayer vias, such as deposition, lithography, and etching processes. It emphasizes the need for precise control and optimization of these fabrication steps to achieve high-quality vias with desired dimensional and geometric characteristics.

In addition, the abstract briefly mentions the characterization methods utilized to assess the structural properties of multilayer vias, such as optical microscopy, scanning electron microscopy (SEM), and atomic force microscopy (AFM). These characterization techniques provide valuable insights into the morphology, surface roughness, and dimensional accuracy of the fabricated vias.

Overall, this abstract serves as a concise overview of the structural analysis and fabrication approach for multilayer vias. It highlights the importance of understanding their structural properties, discusses key fabrication techniques, and briefly mentions the characterization methods used to assess their quality. This information provides a foundation for further research and development in the field of multilayer via technology.

Contents

List of Figures

List of Tables

Chapter 1

Superconductivity

Superconductivity is a fascinating and complex phenomenon in which certain materials can conduct electricity with zero resistance at low temperatures. This unique property has the potential to revolutionize a wide range of fields, from energy transmission and storage to medical imaging and high-speed computing. The discovery of superconductivity in 1911 by Heike Kamerlingh Onnes marked a major breakthrough in the field of condensed matter physics and has led to a greater understanding of the behavior of electrons in materials[1].

The behavior of electrons in superconducting materials is fundamentally different from their behavior in normal conductors. In normal conductors, such as copper wires, electrons are scattered by the vibrations of the atoms in the material, leading to resistance and the production of heat. In contrast, in superconducting materials, electrons form pairs known as Cooper pairs, which move through the material with zero resistance. This occurs due to the interaction between the electrons and the lattice of the material, which produces a distortion in the lattice that allows the Cooper pairs to move without resistance. This results in a highly efficient transfer of electrical energy and has the potential to drastically reduce energy loss in power transmission and storage[2].

The discovery of superconductivity has also led to the development of a wide range of groundbreaking technologies. For example, superconducting magnets are used in magnetic resonance imaging (MRI) machines for medical diagnosis, as well as in particle accelerators for scientific research. In addition, the Josephson effect, discovered in 1962 by Brian Josephson, involves the tunneling of superconducting electrons through a thin insulating layer between two superconducting materials, resulting in the formation of a Josephson junction. Josephson junctions have been used in a wide range of applications, including in the development of superconducting quantum interference devices (SQUIDs) for magnetic field detection and in the development of superconducting qubits for quantum computing[3].

Despite the many potential applications of superconductivity, there are still many challenges that need to be addressed before it can be widely applied in practical situations. One of the main challenges is the need to maintain low temperatures in order to achieve superconductivity. This has led to the development of cryogenic cooling systems that use liquid helium or liquid nitrogen to maintain the low temperatures required for superconductivity. Another challenge is the cost and complexity of superconducting materials and devices, which limit their widespread use in many applications[2].

Nevertheless, the continued research and development in the field of superconductivity holds the promise of unlocking new technologies and changing the way we live and work. The study of superconductivity has led to the discovery of many other novel and fascinating phenomena, including the Meissner effect, which involves the expulsion of magnetic fields from superconducting materials. As we continue to unlock the secrets of superconductivity, we may be able to develop new materials and devices that could revolutionize fields ranging from transportation to energy production and beyond.

1.1 Theories of Superconductivity

While the discovery of superconductivity was initially met with skepticism and skepticism, it has since become one of the most extensively studied topics in condensed matter physics. Theories in superconductivity seek to explain the underlying mechanisms that give rise to this unique and highly desirable property.

One of the most fundamental theories of superconductivity is the Bardeen-Cooper-Schrieffer (BCS) theory, which was proposed in 1957 by John Bardeen, Leon Cooper, and John Schrieffer. The BCS theory suggests that at low temperatures, electrons in a superconducting material form pairs known as Cooper pairs. These Cooper pairs are held together by the exchange of phonons, which are the vibrational modes of the lattice structure of the material. The formation of Cooper pairs allows electrons to move through the material with zero resistance, resulting in superconductivity[4].

Another important theory in superconductivity is the Ginzburg-Landau (GL) theory, which was proposed in 1950 by Vitaly Ginzburg and Lev Landau. The GL theory provides a more macroscopic approach to understanding superconductivity by describing the behavior of the superconducting order parameter, which describes the degree of coherence of the Cooper pairs in the material. The GL theory also predicts the existence of the Meissner effect, which involves the expulsion of magnetic fields from a superconducting material[5].

In addition to these two major theories, there are also several other theories that seek to explain different aspects of superconductivity. For example, the Anderson-Higgs mechanism, proposed in 1963 by Philip Anderson, suggests that the symmetry-breaking mechanism that leads to superconductivity is similar to the mechanism that gives particles mass in the Higgs boson theory. Another theory, the high-temperature superconductivity theory, seeks to explain the superconductivity that occurs at temperatures above the boiling point of liquid nitrogen. This type of superconductivity was first observed in the 1980s and remains a topic of intense research to this day[6].

Despite the many theories that have been proposed, there are still many unanswered questions about the underlying mechanisms of superconductivity. For example, it is not yet fully understood how Cooper pairs are able to move through a material without resistance, or why certain materials exhibit superconductivity while others do not. This has led to ongoing research and debate in the field of superconductivity, with the aim of developing a more complete understanding of this fascinating phenomenon[7].

In conclusion, the study of superconductivity has been a fascinating journey, filled with many groundbreaking discoveries and theories. The BCS and GL theories are just two examples of the many different theories that have been proposed to explain this unique phenomenon.

1.1.1 Electron Paired Bound State

An electron paired bound state is a fundamental concept in superconductivity. When a material is cooled to a temperature below a critical temperature, typically several Kelvin or below, the electrons in the material begin to exhibit unique behavior. At this low temperature, the electrons begin to form pairs, known as Cooper pairs, which can move through the material with zero resistance[5].

The formation of these Cooper pairs can be explained by the Bardeen-Cooper-Schrieffer (BCS) theory. According to the BCS theory, the Cooper pairs form due to the exchange of phonons, which are the vibrational modes of the lattice structure of the material. As an electron moves through the lattice, it interacts with the lattice ions, which can cause the electron to emit a phonon. The emitted phonon can then interact with another nearby electron, causing it to absorb the phonon and move closer to the first electron. This process can repeat, with the two electrons becoming more and more tightly bound until they form a Cooper pair[4].

The formation of the Cooper pairs has important consequences for the electrical properties of the material. Because the electrons are now paired, they can move through the material with zero resistance. This is because as one electron moves through the lattice, it can drag its partner along with it, without experiencing any resistance from the lattice[2]. The resistance-free movement of electrons is the hallmark of superconductivity and has many important practical applications, such as in the construction of powerful magnets and in energy-efficient power transmission[4].

The existence of the electron paired bound state has been experimentally verified and is a subject of ongoing research and study. Researchers are working to better understand the underlying mechanisms that give rise to this phenomenon and to develop new materials that exhibit superconductivity at higher temperatures. While the BCS theory provides a good description of the formation of the Cooper pairs, there are still many unanswered questions about the details of this process[4].

1.1.2 BCS Ground State

The BCS ground state is a concept in superconductivity that can be described using equations and figures. It refers to the lowest-energy state of a superconductor, in which Cooper pairs of electrons are formed and condensed into a macroscopic quantum state. The BCS theory explains the formation of this ground state in terms of the interaction of electrons with each other and with the lattice of the material[4].

The BCS theory can be summarized using the following equation:

$$\Delta(k) = -\frac{1}{N(0)} \sum_{k'} V(k,k') \frac{\Delta(k')}{2E(k')} tanh\left(\frac{E(k')}{2k_B T}\right) \tag{1.1}$$

where $\Delta(k)$ is the energy gap function, which describes the energy required to break up a Cooper pair. $V(k,k')$ is the attractive potential between electrons due to the exchange of phonons, $N(0)$ is the density of states at the Fermi level, $E(k)$ is the energy of an electron with momentum k, and k_B is the Boltzmann constant[8].

The BCS ground state can also be visualized using a plot of the energy bands of a superconductor. The energy bands of a normal metal are separated by a gap at the Fermi level, which represents the energy required to excite an electron from the filled states to

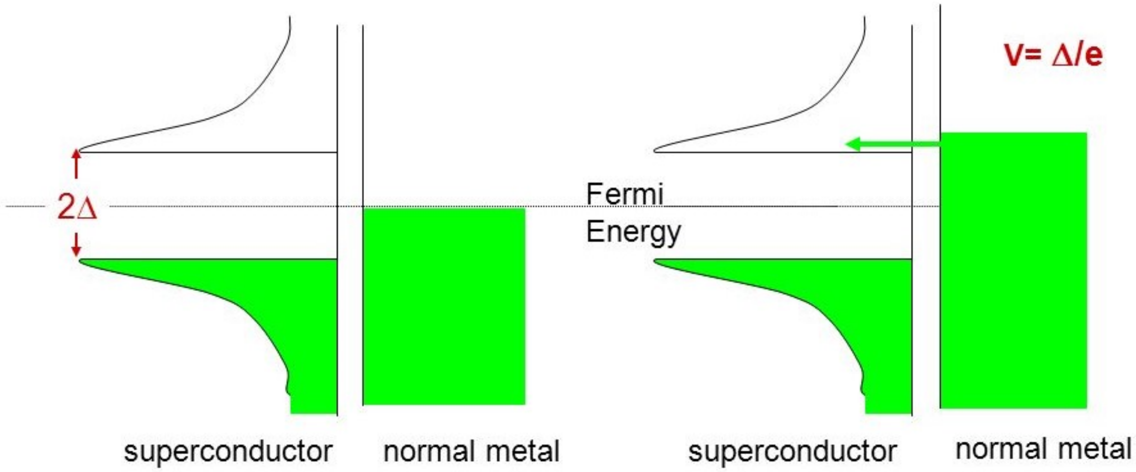

Figure 1.1: Superconductor versus Normal Metal

the empty states. In a superconductor, this gap is filled by Cooper pairs, which results in a single energy band. This can be seen in the figure above, which shows the energy bands of a superconductor at different temperatures[4].

At high temperatures, the energy bands of a superconductor resemble those of a normal metal, with a gap at the Fermi level. As the temperature decreases, the energy gap begins to fill with Cooper pairs, and the energy bands start to merge. At the critical temperature, the energy bands merge completely, resulting in a single energy band and the formation of the BCS ground state[4].

In summary, the BCS ground state is a macroscopic quantum state in which Cooper pairs of electrons are condensed into a single energy band. This state can be described using equations, such as the BCS gap equation, and can be visualized using plots of the energy bands of a superconductor. The BCS theory provides a framework for understanding the formation of this ground state, which is a key feature of superconductivity[9].

1.1.3 Superconducting Order Parameter

The superconducting order parameter is a key concept in the theory of superconductivity, and it provides a fundamental understanding of the behavior of superconductors in magnetic fields, in the presence of defects, and in other complex situations[10]. The order parameter is a complex-valued wave function that describes the coherent motion of Cooper pairs in a superconductor. It is defined as the expectation value of the pair-creation operator, which is the difference between the probability of finding a pair in the ground state and the probability of finding it in the absence of the pair. In mathematical terms, the order parameter is given by:

$$\Delta(\mathbf{r}) = \langle \Psi | c_{i\uparrow} c_{i\downarrow} | \Psi \rangle, \tag{1.2}$$

where $\Delta(\mathbf{r})$ is the order parameter as a function of position $\mathbf{r}$, $|\Psi\rangle$ is the ground state wave function of the superconductor, and $c_{i\uparrow}$ and $c_{i\downarrow}$ are the creation operators for electrons with opposite spin. The order parameter is a complex quantity because it describes a coherent superposition of two electrons with opposite spin and momentum[11].

The magnitude of the order parameter is related to the energy gap in the electronic spectrum of the superconductor, and it plays a key role in determining the superconducting properties of the material. The order parameter vanishes at the transition temperature, T_c, above which the superconductor becomes a normal conductor. Below T_c, the order parameter is finite, and it gives rise to the Meissner effect, whereby a superconductor expels magnetic fields from its interior.

The order parameter can be written in terms of its magnitude, $|\Delta(\mathbf{r})|$, and phase, $\theta(\mathbf{r})$, as:

$$\Delta(\mathbf{r}) = |\Delta(\mathbf{r})|e^{i\theta(\mathbf{r})} \tag{1.3}$$

The magnitude $|\Delta(\mathbf{r})|$ is related to the energy gap, ΔE, via the relation:

$$|\Delta(\mathbf{r})| = \sqrt{\frac{2\Delta E(\mathbf{r})}{\pi}} \tag{1.4}$$

where $\Delta E(\mathbf{r})$ is the energy gap at position $\mathbf{r}$. The phase $\theta(\mathbf{r})$ is related to the supercurrent density, $\mathbf{j}(\mathbf{r})$, by the relation:

$$\theta(\mathbf{r}) = 2e \int_C \mathbf{j}(\mathbf{r}') \cdot d\mathbf{r}' \tag{1.5}$$

where e is the electron charge and the integral is taken over a closed loop C in the superconductor. The phase of the order parameter is responsible for the Josephson effect, whereby a supercurrent flows between two superconductors separated by a thin insulating barrier.

The order parameter is also related to the coherence length, ξ which is a measure of the distance over which the order parameter decays. The coherence length is given by:

$$\xi = \frac{\hbar v_F}{\pi \Delta_E} \tag{1.6}$$

where $\hbar$ is the reduced Planck constant and v_F is the Fermi velocity. The coherence length is an important parameter in determining the behavior of the superconductor in the presence of impurities or defects.

Overall, the superconducting order parameter is a key concept in the theory of superconductivity, and it provides a fundamental understanding of the behavior of superconductors in magnetic fields, in the presence of defects, and in other complex situations. Figure 1.2 shows a schematic representation of the order parameter and its relation to the energy gap and coherence length[12].

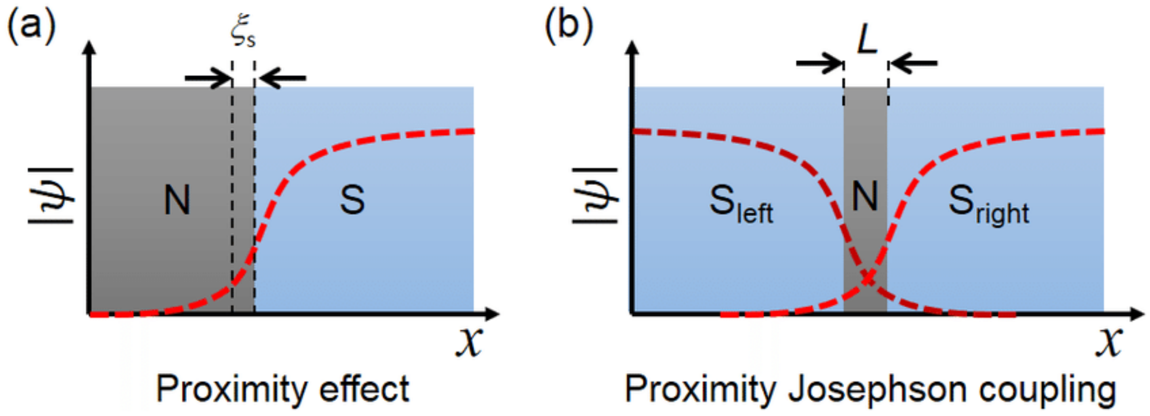

Figure 1.2: Schematic representation of the superconducting order parameter, its relation to the energy gap and coherence length, and its role in determining the behavior of a superconductor.

1.2 Electrons and Phonons in Superconductivity

1.2.1 Interaction between Electrons and Phonons

In conventional superconductors, the dominant mechanism for electron pairing is the interaction between electrons and phonons, which are lattice vibrations. The interaction can be described by the electron-phonon coupling constant λ, which measures the strength of the interaction. The coupling constant is given by:

$$\lambda = \frac{2}{N(0)V} \sum_{\mathbf{k},\mathbf{q}} \frac{|\langle \mathbf{k}+\mathbf{q}|\mathbf{k}\rangle|^2}{\omega_{\mathbf{q}}}, \tag{1.7}$$

where $N(0)$ is the density of states at the Fermi level, V is the volume of the crystal, $\mathbf{k}$ and $\mathbf{q}$ are wave vectors, $\omega_{\mathbf{q}}$ is the phonon frequency, and $\langle \mathbf{k}+\mathbf{q}|\mathbf{k}\rangle$ is the electron-phonon matrix element[13].

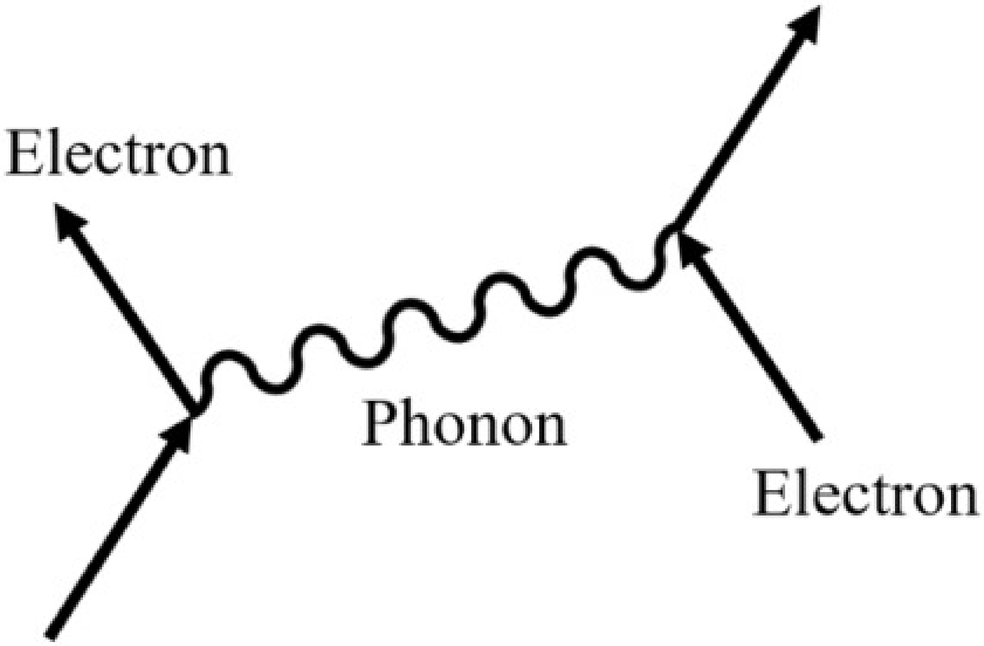

Figure 1.3: Illustration of the interaction between electrons and phonons in a superconductor. The exchange of phonons can lead to the formation of Cooper pairs, which are bound together by the attractive interaction mediated by the phonons.

1.2.2 Cooper Pairing Mechanisms

The electron-phonon interaction leads to the formation of Cooper pairs, which are pairs of electrons that are bound together by the exchange of phonons[14]. The formation of Cooper pairs is described by the BCS theory, which proposes that the ground state of a superconductor is a condensate of Cooper pairs[15].

The BCS theory predicts that the energy gap, Δ, which is the minimum amount of energy required to break a Cooper pair, is related to the electron-phonon coupling constant by:

$$\Delta = 1.76\omega_D \exp\left(-\frac{1}{\lambda}\right), \tag{1.8}$$

where ω_D is the Debye frequency. The energy gap is also related to the critical temperature, T_c, by:

$$\Delta = 3.52 k_B T_c, \tag{1.9}$$

where k_B is the Boltzmann constant.

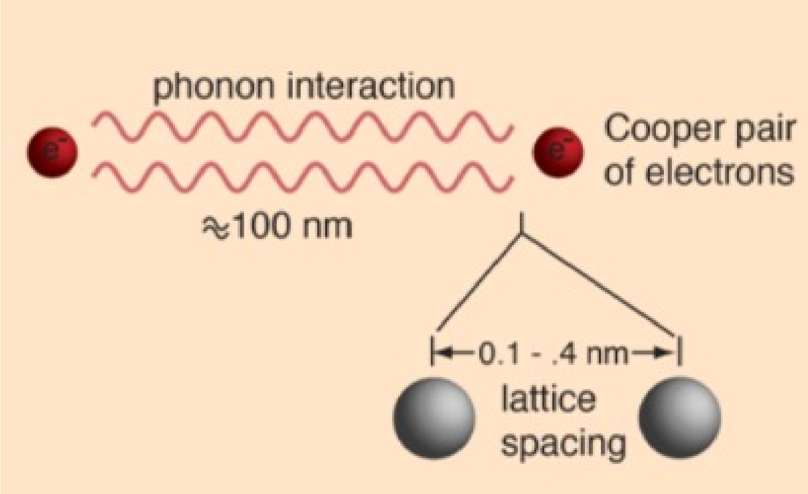

Figure 1.4: The behavior of superconductors suggests that electron pairs are coupling over a range of hundreds of nanometers, three orders of magnitude larger than the lattice spacing these phenomenon is called cooper pairs

1.2.3 Role of Crystal Lattice in Superconductivity

The crystal lattice plays an important role in determining the properties of a superconductor. In particular, the crystal structure can affect the strength of the electron-phonon coupling and the magnitude of the energy gap[16].

For example, in the case of high-temperature superconductors, the crystal structure contains layers of copper oxide separated by insulating layers. The electronic properties of the copper oxide layers are strongly influenced by the lattice vibrations of the oxygen atoms, which can lead to a high electron-phonon coupling constant and a large energy gap[17].

1.2.4 Effect of Impurities and Disorder on Superconductivity

In dirty or disordered superconductors, the electrons and phonons are more likely to scatter off impurities or defects in the crystal lattice[18]. This can lead to a reduction in the electron-phonon coupling constant and the energy gap, which can result in a decrease in the critical temperature[19].

However, it is possible for the presence of impurities or defects to have the opposite effect, by introducing additional electronic states near the Fermi level that can enhance the electron-phonon interaction[20]. This can lead to an increase in the electron-phonon coupling constant and the energy gap, and potentially an increase in the critical temperature[21].

1.3 Electron Tunelling

Electron tunneling is a quantum mechanical phenomenon in which an electron can pass through a potential barrier that would be classically forbidden[22]. This process occurs when two conducting materials are separated by a thin insulating layer, and a voltage is applied across the structure[23].

The tunneling current I through a thin insulating barrier of thickness d can be described by the following equation:

$$I = \frac{Aq}{\hbar}\frac{2m^*}{\pi\hbar^2}\int_0^\infty T(E)[f(E-eV_1)-f(E-eV_2)]dE \tag{1.10}$$

where A is the area of the tunneling junction, q is the charge of an electron, $\hbar$ is the reduced Planck constant, m^* is the effective mass of the electrons in the electrodes, $T(E)$ is the transmission probability of an electron with energy E, $f(E-eV)$ is the Fermi-Dirac distribution function, V_1 is the bias voltage on one side of the tunneling barrier, and V_2 is the bias voltage on the other side of the barrier[24].

The transmission probability $T(E)$ can be calculated from the wave functions of the electrons in the electrodes and the potential barrier. In the case of a rectangular potential barrier, the transmission probability is given by:

$$T(E) = \frac{4k_1k_2}{(k_1+k_2)^2}\cos^2(k_2d) \tag{1.11}$$

where k_1 and k_2 are the wavevectors of the electrons in the electrodes and the barrier, respectively, and d is the thickness of the barrier.

The tunneling current depends exponentially on the thickness of the insulating barrier and the height of the potential barrier. This dependence is described by the following equation:

$$I \propto \exp\left(-\frac{2d}{\hbar}\sqrt{2m^*(V_1 + V_2 - E)}\right) \tag{1.12}$$

where E is the energy of the electrons that are tunneling through the barrier.

The tunneling current can be measured experimentally by applying a small voltage across the tunneling junction and measuring the resulting current. The magnitude of the tunneling current can be used to extract information about the electronic structure of the materials and the potential barrier[24].

Figure 1.5 shows a schematic diagram of a tunneling junction and the potential barrier that electrons must tunnel through. The figure also shows the dependence of the tunneling current on the thickness of the insulating barrier and the height of the potential barrier.

1.4 Long Range Coherence

Long-range coherence is a key feature of Bose-Einstein condensates (BECs), which are a state of matter that arises when a collection of bosons, a type of quantum particle, is cooled to very low temperatures. In a BEC, a large number of particles occupy the same quantum state, leading to quantum mechanical effects that are not observable in classical physics[25].

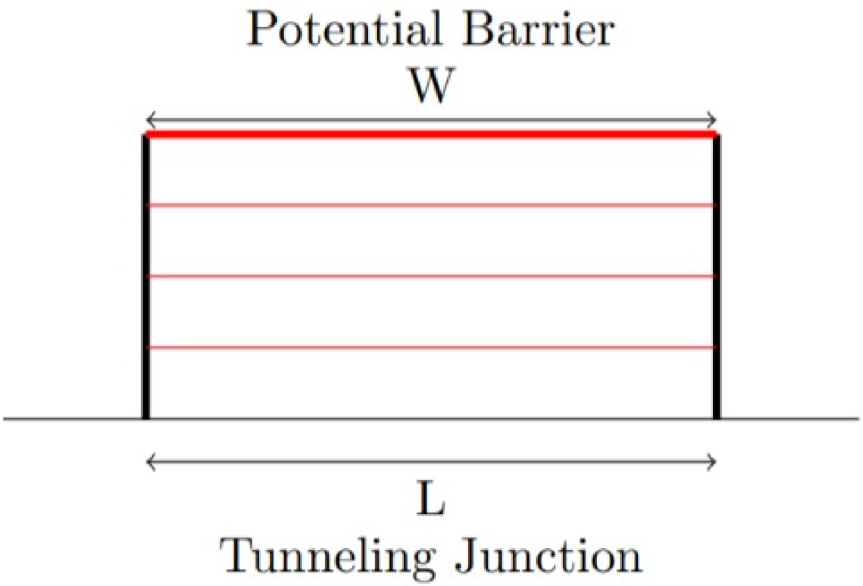

Figure 1.5: Schematic diagram of a tunneling junction and the potential barrier that electrons must tunnel through. The figure also shows the dependence of the tunneling current on the thickness of the insulating barrier and the height of the potential barrier.

In the case of a BEC, long-range coherence refers to the fact that all of the particles in the condensate are in the same quantum state, and that the wave function describing the condensate extends coherently over macroscopic distances. This means that the phase of the wave function at any point in space is the same as the phase at any other point in space, and that the condensate can exhibit interference effects, such as the interference pattern seen in the double-slit experiment[26].

Mathematically, long-range coherence in a BEC is described by the off-diagonal long-range order (ODLRO) of the one-particle density matrix, which is a measure of the correlations between the positions of the particles in the condensate. The ODLRO is defined as:

$$g^{(1)}(\vec{r_1}, \vec{r_2}) = \langle \Psi^{\dagger}(\vec{r_2}) \Psi(\vec{r_1}) \rangle \tag{1.13}$$

where $\Psi^\dagger(\vec{r})$ and $\Psi(\vec{r})$ are the creation and annihilation operators for the particles in the condensate, and the angle brackets denote an ensemble average. The ODLRO indicates the degree to which the particles in the condensate are correlated in position space, and it is a measure of the coherence of the condensate[27].

Figure1.6 shows the density profile of a BEC in the ground state, where the particles are in the same quantum state and exhibit long-range coherence. The density profile shows the probability of finding a particle at a given position in space, and it is a signature of the spatial coherence of the condensate.

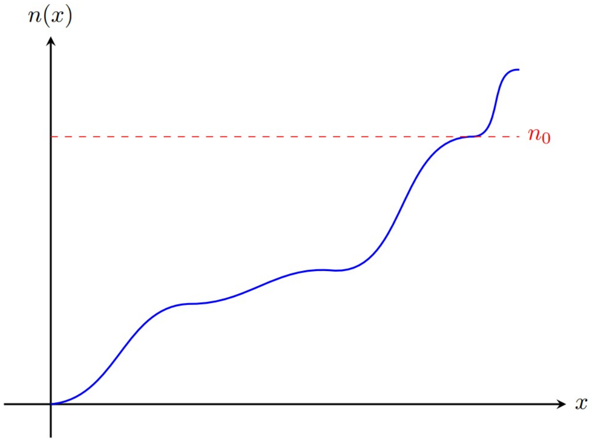

Figure 1.6: Density profile of a Bose-Einstein condensate in the ground state.

Long-range coherence is an important property of BECs because it allows for the observation of quantum mechanical effects on a macroscopic scale, and it has potential applications in precision measurement, quantum computing, and other areas of research[28].

1.5 Josephson Effect

The Josephson effect is a quantum mechanical phenomenon in which a supercurrent flows between two superconductors separated by a thin insulating barrier, known as a Josephson junction[29]. This effect was first predicted by Brian Josephson in 1962, and has since been studied extensively due to its fundamental importance and potential applications in quantum information processing.

The Josephson effect is based on the ability of superconducting electrons to tunnel through the insulating barrier, resulting in a non-zero probability of finding an electron on the other side. This leads to a flow of supercurrent between the two superconductors, even in the absence of an applied voltage. The magnitude of the supercurrent is given by the Josephson relation:

$$I = I_c \sin(\delta) \tag{1.14}$$

where I_c is the critical current of the junction and δ is the phase difference between the superconducting wave functions on either side of the junction. The phase difference is related to the time derivative of the phase across the junction, $\dot{\delta} = 2\pi V/\Phi_0$, where V is the voltage across the junction and Φ_0 is the flux quantum[30].

The Josephson effect has been studied in a variety of experimental settings, including in superconducting quantum interference devices (SQUIDs), which are used for extremely sensitive magnetic field measurements. In addition, the Josephson effect has been used in the development of superconducting qubits, which are the building blocks of quantum computers[31].

Figure1.7 shows a schematic of a Josephson junction. The junction consists of two superconductors separated by a thin insulating barrier, which allows for the tunneling of superconducting electrons between the two sides. The phase difference across the junction, δ, determines the magnitude and direction of the supercurrent, which can be measured using a variety of experimental techniques[32].

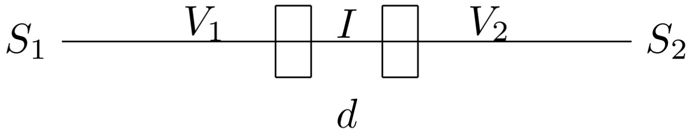

Figure 1.7: Schematic of a Josephson junction, consisting of two superconductors separated by a thin insulating barrier. The phase difference across the junction determines the magnitude and direction of the supercurrent.

1.5.1 Resistively Capacitively Shunted Junction (RCSJ) Model

The Resistively Capacitively Shunted Junction (RCSJ) model is a theoretical model used to describe the behavior of Josephson junctions, which are devices that exhibit superconducting properties. The model assumes that the junction is made up of two superconducting electrodes separated by a thin insulating barrier, and that the electrodes are connected by a shunt circuit consisting of a resistor and a capacitor.

The behavior of the Josephson junction is governed by the Josephson effect, which is the phenomenon where a supercurrent flows across the insulating barrier due to a phase difference between the superconducting electrodes[33]. This phase difference is related to the voltage across the junction by the Josephson relation:

$$V = \frac{\hbar}{2e}\frac{d\phi}{dt} \tag{1.15}$$

where V is the voltage across the junction, $\hbar$ is the reduced Planck constant, e is the elementary charge, and ϕ is the phase difference.

The RCSJ model includes two additional equations to describe the behavior of the shunt circuit. The first equation is Ohm's law, which relates the voltage across the resistor to the current through it:

$$V_R = IR \tag{1.16}$$

where V_R is the voltage across the resistor, I is the current through it, and R is the resistance of the shunt circuit.

The second equation is the capacitor equation, which relates the current through the capacitor to the rate of change of the voltage across it:

$$I_C = C\frac{dV_C}{dt} \tag{1.17}$$

where I_C is the current through the capacitor, V_C is the voltage across it, and C is the capacitance of the shunt circuit.

Using these equations, the RCSJ model can be used to calculate the voltage and current across the Josephson junction as a function of time. The model predicts a variety of behaviors, including the presence of oscillations in the voltage and current, and the existence of a critical current below which the junction behaves as a resistor[34].

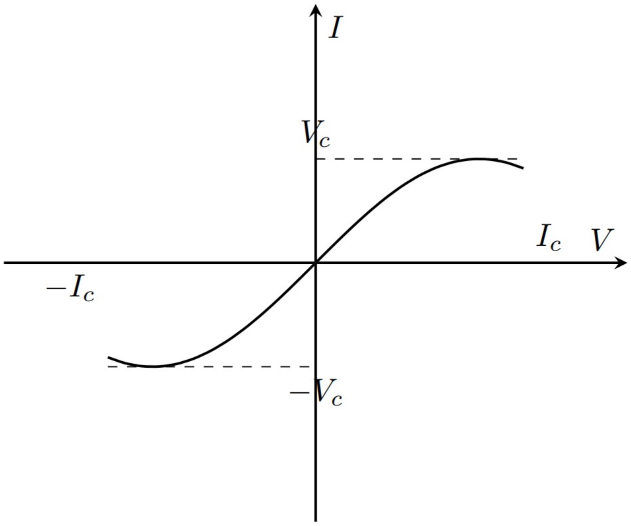

Figure 1.8: Current-voltage characteristic of a Josephson junction using the RCSJ model. The critical current I_c and critical voltage V_c are shown as dashed lines.

The behavior of the junction can be visualized using graph. For example, Figure 1.8 a plot of the voltage across the junction as a function of time can reveal the presence of oscillations. Similarly, a plot of I-V characteristic of the junction show the existence of I_c.

1.5.2 Magnetic Flux Effects

In Josephson junctions, the supercurrent flowing through the junction is directly related to the phase difference between the two superconducting electrodes. The phase difference can be influenced by an external magnetic field, which can have several effects on the behavior of the junction.

One of the most important effects of a magnetic field is to induce a voltage across the junction, known as the AC Josephson effect. This effect occurs when an oscillating magnetic field is applied to the junction, and the resulting voltage oscillates at the same frequency as the magnetic field. The voltage oscillations are proportional to the frequency of the magnetic field, and the proportionality constant is known as the Josephson constant.

In addition to the AC Josephson effect, a magnetic field can also induce a static voltage across the junction, known as the DC Josephson effect. This effect occurs when a constant magnetic field is applied to the junction, and the resulting voltage is proportional to the strength of the magnetic field. The proportionality constant is known as the magnetic flux quantum, and is a fundamental constant of nature.

The magnetic field can also affect the critical current of the junction, which is the maximum supercurrent that can flow through the junction without inducing a voltage. The critical current is reduced by the presence of a magnetic field, and this reduction is known as the Fraunhofer pattern. The Fraunhofer pattern is a series of peaks and valleys in the critical current as a function of the magnetic field strength, and is caused by the interference of the superconducting waves in the two electrodes[32].

To illustrate these effects, Figure 1.9 shows a schematic of a Josephson junction with an external magnetic field applied to it, and the resulting voltage and critical current as a function of the magnetic field strength.

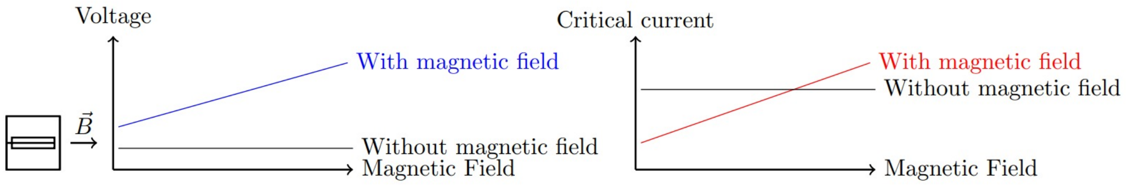

Figure 1.9: Schematic of a Josephson junction with an external magnetic field applied to it, and the resulting voltage and critical current as a function of the magnetic field strength.

The equations governing the behavior of a Josephson junction in the presence of a magnetic field are given by the resistively shunted junction (RSJ) model, which includes the effects of the magnetic field on the voltage and critical current. The RSJ model is a differential equation that can be solved numerically to obtain the voltage and current as a function of time and magnetic field strength.

1.5.3 Fiske Modes

Fiske modes are the resonant oscillations of the voltage across a Josephson junction in response to an external microwave signal. These oscillations occur when the frequency of the microwave signal is a multiple of the Josephson frequency, which is determined by the critical current and the capacitance of the junction. The presence of Fiske modes can be used to study the properties of Josephson junctions and to develop devices for microwave signal processing[35].

The equations that describe the Fiske modes in a Josephson junction are:

$$I_c = I_c^0 \cos\left(\frac{2\pi\Phi}{\Phi_0} + \delta\right) \tag{1.18}$$

where I_c is the critical current of the junction, I_c^0 is the maximum critical current, Φ is the magnetic flux through the junction, Φ_0 is the flux quantum, and δ is the phase difference across the junction[36].

The presence of Fiske modes can be visualized using graph. For example, Figure 1.12 a plot of the voltage across the junction as a function of the frequency of the microwave signal can show the resonant peaks associated with the Fiske modes[37]. Similarly, a power-frequency plot displays resonant peaks in the absorbed power.

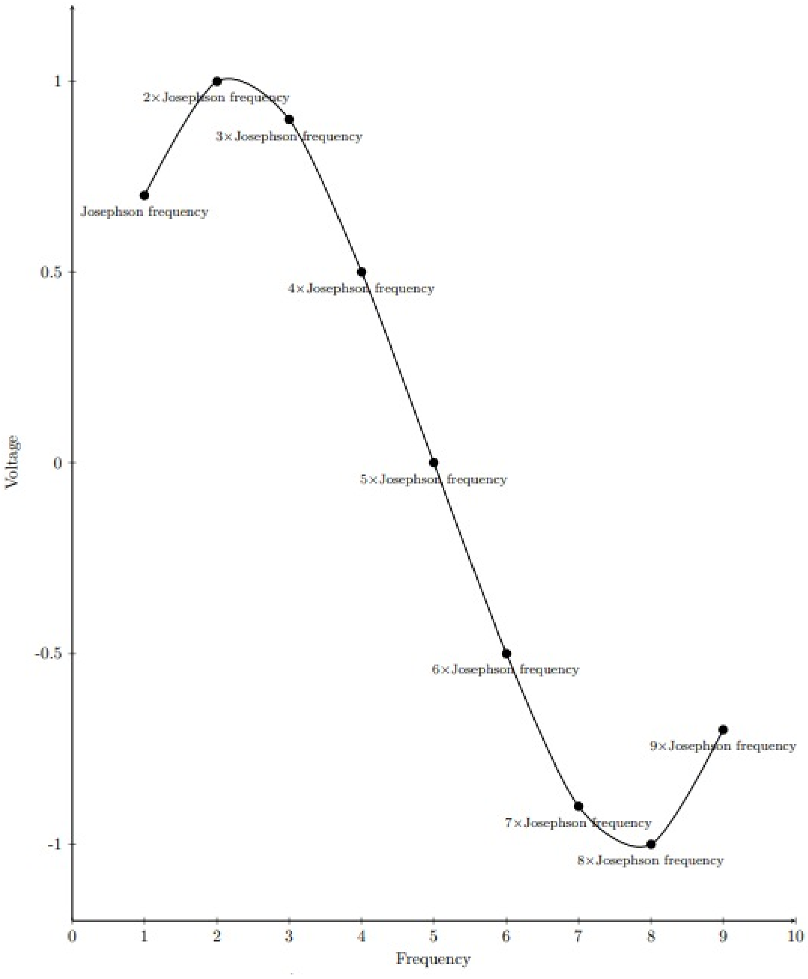

Figure 1.10: Plot of the voltage across a Josephson junction as a function of the frequency of the microwave signal, showing the resonant peaks associated with the Fiske modes.

In this plot, the x-axis represents the frequency of the microwave signal, and the y-axis represents the voltage across the junction. The resonant peaks occur at frequencies that are multiples of the Josephson frequency, as predicted by the Fiske modes theory.

Overall, the study of Fiske modes in Josephson junctions is an important area of research in the field of superconductivity, with a wide range of potential applications in microwave signal processing and quantum information processing[38].

1.5.4 AC Biased Josephson Junction

AC biased Josephson junctions are a type of superconducting device that can be used as sensitive detectors of electromagnetic radiation, as well as for a variety of other applications in quantum information processing and metrology[39]. An AC biased Josephson junction consists of a thin barrier of insulating material sandwiched between two superconducting electrodes, which can be biased with an AC voltage signal.

The dynamics of an AC biased Josephson junction can be described by the resistively and capacitively shunted junction (RCSJ) model, which includes both the Josephson tunneling current and the capacitive charging current. The current-voltage relationship of the junction is given by the RSFQ (rapid single flux quantum) model:

$$I_J = I_c \sin(\phi) + \frac{\hbar C}{2e}\frac{d\phi}{dt} + I_{ext} \tag{1.19}$$

where I_J is the Josephson tunneling current, I_c is the critical current of the junction, ϕ is the phase difference between the two superconducting electrodes, C is the capacitance of the junction, e is the elementary charge, $\hbar$ is the reduced Planck constant, $d\phi/dt$ is the time derivative of the phase difference, and I_{ext} is the externally applied current[40].

The voltage across the junction can be obtained from the time derivative of the phase difference:

$$V_J = \frac{\hbar}{2e}\frac{d^2\phi}{dt^2} \tag{1.20}$$

When the junction is biased with an AC voltage signal, it can exhibit a variety of interesting phenomena, including Shapiro steps, Fiske steps, and photon-assisted

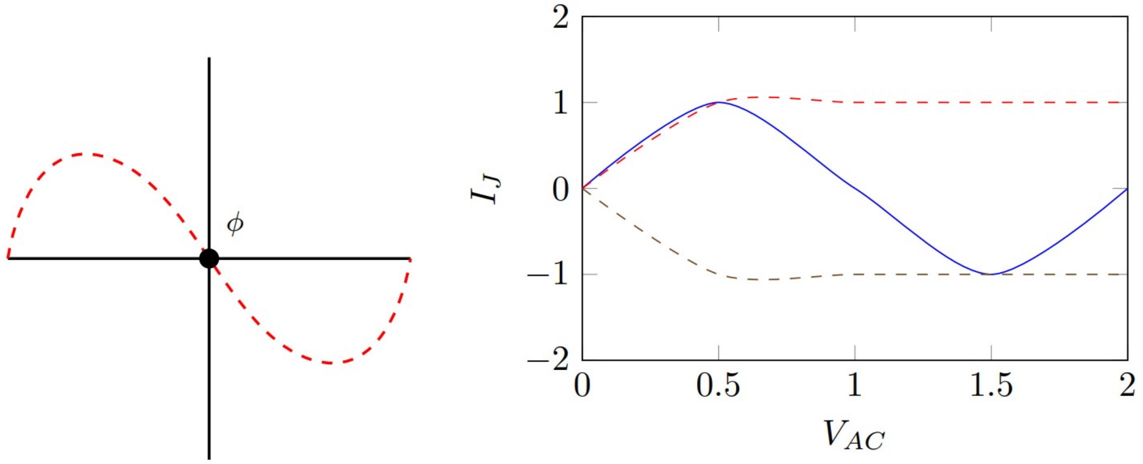

Figure 1.11: Schematic diagram of an AC biased Josephson junction (left) and current-voltage characteristic of the junction for different values of the AC amplitude (right). As the amplitude of the AC signal is increased, the current-voltage characteristic becomes more complex, exhibiting a series of steps and plateaus that correspond to different resonant modes of the junction.

tunneling[35]. These effects arise due to the nonlinear response of the junction to the applied voltage, and can be used to detect and manipulate electromagnetic radiation with high sensitivity[41].

Figure 1.11 shows a schematic diagram of an AC biased Josephson junction, as well as a plot of the current-voltage characteristic of the junction for different values of the AC amplitude. As the amplitude of the AC signal is increased, the current-voltage characteristic becomes more complex, exhibiting a series of steps and plateaus that correspond to different resonant modes of the junction. These resonant modes can be used for a variety of applications, including high-frequency signal detection and quantum information processing[42].

1.6 Superconducting Quantum Interference Devices

A superconducting quantum interference device (SQUID) is a type of quantum sensor that uses the unique properties of superconductivity to detect very small magnetic fields. SQUIDs are based on the Josephson effect, in which a supercurrent can flow through a weak link between two superconductors, even in the absence of a voltage difference. The basic structure of a SQUID consists of a loop of superconducting wire interrupted by one or more Josephson junctions.

The current in the loop can be controlled by an external magnetic field, and the SQUID is highly sensitive to changes in this magnetic field. In fact, SQUIDs are the most sensitive magnetic field detectors available, capable of measuring magnetic fields down to femtotesla 10^{-15}T levels.

The voltage across a SQUID can be described by the Josephson relations:

$$V = \frac{\hbar}{2e}\frac{d\phi}{dt} \tag{1.21}$$

$$I = I_c \sin(\phi) \tag{1.22}$$

where V is the voltage across the SQUID, ϕ is the phase difference across the Josephson junction, I is the current through the SQUID, I_c is the critical current of the junction, e is the elementary charge, and $\hbar$ is the reduced Planck constant.

The behavior of a SQUID can be understood by considering the two possible states of the junction: a state in which the phase difference across the junction is zero, and a state in which the phase difference is π. The energy difference between these two states is proportional to the magnetic flux through the SQUID loop. When the magnetic flux changes, the SQUID can switch between these two states, resulting in a change in the voltage across the SQUID.

There are two main types of SQUIDs: radio-frequency (RF) SQUIDs and direct-current (DC) SQUIDs.

RF SQUIDs use a resonant circuit to achieve a high sensitivity to magnetic fields. The resonant circuit consists of a superconducting loop interrupted by a Josephson junction, which is capacitively coupled to an input coil. When a magnetic field is applied to the input coil, it induces a current in the resonant circuit, which produces a voltage across the junction. This voltage can be read out and used to measure the magnetic field. RF SQUIDs are typically operated at liquid helium temperatures, around 4 K.

DC SQUIDs, on the other hand, use a superconducting loop interrupted by two Josephson junctions in series. The input coil is connected to the loop, and when a magnetic field is applied, it induces a circulating current in the loop. The two junctions act as non-linear inductors, and the resulting voltage across the SQUID can be measured to determine the magnetic flux through the input coil. DC SQUIDs are typically operated at a slightly higher temperature than RF SQUIDs, around 4.2 K.

A common configuration of the SQUID is the dc SQUID, which is operated at a constant bias current. The voltage across the SQUID is monitored as a function of the applied magnetic field, and the resulting signal is highly sensitive to small changes in the magnetic field[32].

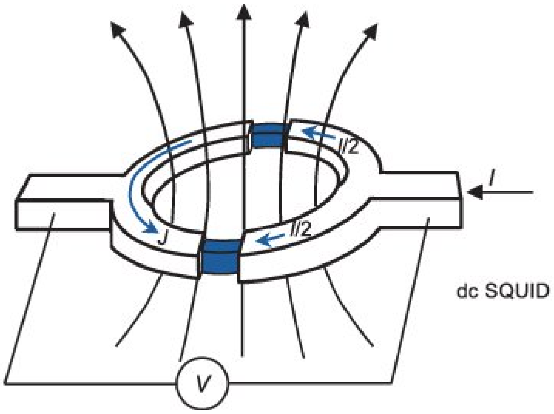

Figure 1.12: Schematic representation of a DC superconducting quantum interference device (SQUID).

1.7 Arrays of Josephson Junction

Arrays of Josephson junctions and SQUIDs are highly researched because the circuits themselves are challenging to measure with responses just above the noise floor[43]. The voltage response of the Josephson devices adds linearly with N devices in series. Moreover, it is predicted that the noise power scales like $\sqrt{N}$, yielding a scaling of the signal-to-noise ratio to be $1/\sqrt{N}$.

Josephson junctions are transducers between voltage and frequency, making series arrays of Josephson junctions the contemporary international standard for defining the volt. A single Josephson junction produces a voltage of the first Shapiro step at ~10 μV, which is difficult in practice to consistently measure. However, the response is scaled up by three orders of magnitude if 1000 Josephson junctions were to be arrayed in series[44].

Responses in the ~mV range are much more suitable to widely available and easily operated semiconductor electronics. Additionally, the voltage response to Josephson phase interference by applied magnetic flux can be engineered by making parallel arrays of

Josephson junctions, leading to the development of the superconducting quantum interference filter (SQIF) that arrays several SQUIDs in parallel, series or in a 2D array, each with different loop dimensions in an attempt to replicate unconventional grating structures in optical physics[45].

The design of arrays of Josephson junctions must be carefully considered to meet the technical design requirements for the specific application.

1.8 Types of Superconductors

The classification of superconductors into type-I and type-II is based on how they respond to magnetic fields. When the strength of the magnetic field exceeds the critical field of H_c, superconductivity can be destroyed. Type-I superconductors have only one critical value, H_c, and can exist in either the normal state, where magnetic flux can penetrate through, or the superconducting state, where all magnetic flux is expelled. Most of the metallic superconductors discovered in the early days belong to this category. In contrast, type-II superconductors have two critical values, H_{c1} and H_{c2}. H_{c1} marks the lower boundary where the material transitions from the superconducting state, where no flux can penetrate, to the mixed state that allows only quantized vortex to exist. As the magnetic field strength increases, H_{c2} represents the higher boundary where the field is strong enough to fully destroy superconductivity and all magnetic field can penetrate the material, like it does in the normal state[46]-[47].

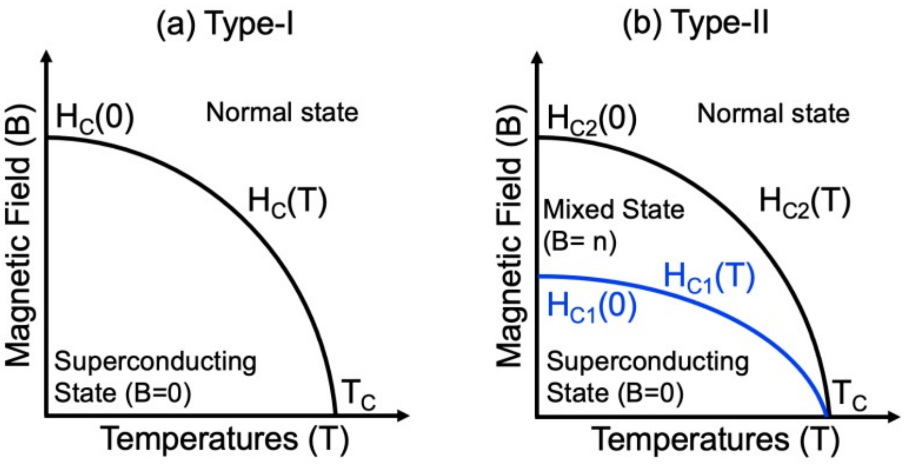

Figure 1.13: Phase diagrams of type-I (a) and type-II (b) superconductors.

1.9 Conventional and Unconventional Superconductors

The categorization of superconductors into conventional and unconventional is based on whether their superconductivity can be explained by the BCS model with the assumption of isotropic s-wave superconductivity. Superconductors that can be described by the BCS model are classified as conventional. Most metallic superconductors discovered in the past are considered conventional. However, there is still debate regarding whether the superconductivity in some materials can be explained by the BCS theory, and such superconductors are known as unconventional. They have gapless quasi-particle excitation spectra instead of clear gap features with sharp edges. The cuprate ceramic copper-oxide superconductors are an example of unconventional superconductors with high anisotropy and V-shaped tunneling spectra[48]-[7].

1.10 Lithography

Lithography is a process used in nanofabrication to create patterns and structures on the surface of materials, such as semiconductors. The process typically involves transferring a pattern from a mask or template to a substrate through a series of steps, including coating, exposure, development, and etching. Lithography has become an essential tool in the production of microelectronic devices, including integrated circuits, microprocessors, and memory chips, as well as in the fabrication of microelectromechanical systems (MEMS), microfluidic devices, and other nanoscale structures.

There are several different types of lithography, including photolithography, electron beam lithography, X-ray lithography, and nanoimprint lithography. Photolithography is the most commonly used type and involves the use of light to transfer a pattern onto the substrate. The process begins with the application of a photosensitive material, or photoresist, onto the substrate. The photoresist is then exposed to light through a mask or template, which contains the desired pattern. The areas of the photoresist that are exposed to light become chemically modified, allowing them to be selectively removed during the development process. The substrate is then etched to create the desired pattern.

Electron beam lithography, on the other hand, uses a focused beam of electrons to transfer a pattern onto the substrate. This technique offers higher resolution than photolithography but is slower and more expensive. X-ray lithography uses X-rays to create the pattern on the substrate, while nanoimprint lithography involves pressing a template into a polymer or other material to create the desired pattern.

Lithography is a critical tool in the field of nanofabrication, enabling the creation of complex patterns and structures with extremely high precision and accuracy. It has played a significant role in the development of the microelectronics industry and continues to be an essential tool in the production of advanced electronic devices and other nanoscale structures.

1.10.1 Photolithography

Conventional lithography is used to print the designed circuit patterns on thin films. The extra material is then removed from the thin films using argon ion milling to transfer the circuit patterns as show in Figure 1.14. In order to create leads to cleaved single crystals, a metal layer is deposited and the metal is left in the desired pattern through a lift-off process. Both thin films and single crystals require the use of lithography to print the required patterns on the samples.

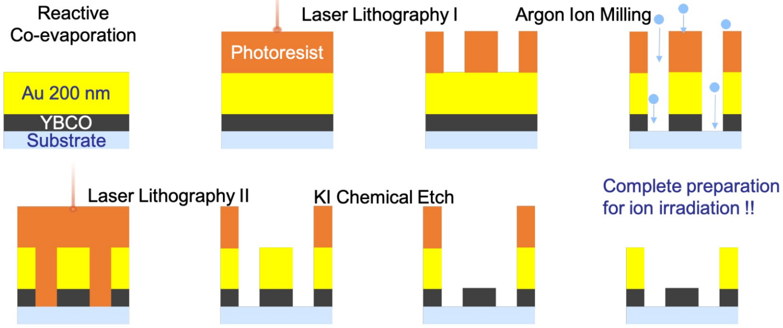

Figure 1.14: Photolithography procedure for YBa2Cu3O7$-\delta$ (YBCO) thin films.

The samples were coated with the photoresist OCG 825 from Fujifilm by spinning at 5000 rpm for 45 seconds. If necessary, the excess solvent can be removed from the photoresist by baking it at 90°C for 1 minute, which makes it harder. For processing single crystals, baking is not required because the substrates will be heated during metal sputtering. The photoresist was then exposed to a g-line laser, which broke the long chemical chains in the exposed regions, making them dissolve when treated with the developer. The residue solvents were washed away with DI water. In order to leave the circuit design on the thin films, the circuit patterns need to be inverted, while the contact pattern can be directly drawn by the laser because the photoresist of the pattern needs to be removed for metal deposition. At this stage, a temporary mask of photoresist was created, which can be washed away if the resulting pattern is problematic, such as due to electrical shorts caused by photoresist residue or broken leads from overdeveloping.

Argon Ion Milling

The circuit pattern was applied to the thin film samples via lithography and then transferred to the films using argon ion milling. To ensure even etching, the samples were mounted on a rotating bronze stage tilted at a 45° angle to prevent dust from settling on the surfaces during milling. A shutter was used to avoid overheating the films during the milling process. The etching time was found to be 90-120 seconds for 30-nm YBCO, 150-200 seconds for 75-nm CeO_2 and about 300 seconds for 200-nm gold (excluding shutter time). To ensure the YBCO film was fully etched without any electrical shorts, electrical continuity was checked at the spare spaces after ion milling. After milling, the first lithography mask was removed using acetone, and the samples were rinsed with isopropanol and dried with nitrogen gas.

Chapter 2

High Transition Temperature Ceramic Oxide Superconductors

High-temperature superconductors (HTS) are materials that exhibit superconductivity at temperatures above the boiling point of liquid nitrogen (77 K), which makes them technologically important for a variety of applications. The discovery of HTS in 1986 in cuprate ceramic oxide materials, specifically the Ba-La-Cu-O system by J.G. Bednorz and K.A. Müller, revolutionized the field of superconductivity[7].

HTS materials are generally classified as unconventional superconductors because they exhibit behaviors that cannot be explained by the conventional BCS theory of superconductivity. The exact mechanism of superconductivity in HTS materials is still not fully understood, and there is active research in this field.

Cuprate ceramic oxide superconductors are one of the most extensively studied HTS materials. They exhibit high transition temperatures, typically above 30 K, and have unique crystal structures that enable the formation of highly anisotropic superconducting states. The cuprate superconductors are often represented by their chemical formula, such as $\mathrm{YBa_2Cu_3O_{7-x}}$ (YBCO), which is one of the most commonly studied cuprate superconductors. Other cuprate superconductors include $\mathrm{La_{2-x}Sr_xCuO_4}$, $\mathrm{Bi_2Sr_2CaCu_2O_{8+x}}$, and $\mathrm{HgBa_2Ca_2Cu_3O_{8+x}}$.

The development of HTS materials has been driven by their potential for practical applications. These include high-field magnets, power transmission, and sensitive detectors. HTS materials also have unique electronic and magnetic properties that make them useful for fundamental research in condensed matter physics. One of the main challenges in the development of HTS materials is their brittle nature, which makes it difficult to manufacture and process them into useful shapes[49].

2.1 Crystal Structure of $\mathrm{YBa_2Cu_3O_{7-\delta}}$

$\mathrm{YBa_2Cu_3O_{7-\delta}}$ (YBCO) is a type of high-temperature superconductor that has been extensively studied since its discovery in 1987. YBCO is a member of a class of materials known as cuprates, which are characterized by the presence of copper-oxide layers in their crystal structure.

One of the most remarkable features of YBCO is its high superconducting transition temperature, which is greater than the boiling point of liquid nitrogen (-196 degrees Celsius). This makes it one of the most promising materials for practical applications of superconductivity, such as in power transmission and magnetic levitation.

YBCO is an orthorhombic perovskite, meaning that its crystal structure is composed of a repeating unit cell that has an elongated, rectangular shape. The unit cell contains copper-oxide chains that run along the b-axis of the crystal, and copper-oxide planes that lie in the a-b plane. The arrangement of these structural units leads to the unique electronic and magnetic properties of YBCO. The unit cell, shown in Figure 2.1, displays both the CuO chains and planes. The lattice parameters commonly cited for YBCO are $a = 3.82$, $b = 3.89$, and $c = 11.68$ $\mathring{A}$[50].

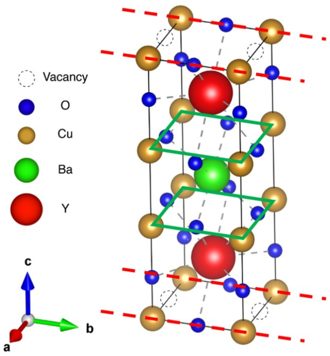

Figure 2.1: The unit cell of $YBa_2Cu_3O_{7-\delta}$ is illustrated, revealing its orthorhombic nature with unequal lattice constants a, b, and c. The crystal symmetry belongs to a subgroup of C_4v. The CuO chains are represented by red dotted lines, and the CuO planes are depicted by green solid lines.

However, YBCO is also a complex material that is prone to defects such as grain boundaries and twinned boundaries. These defects can significantly impact the transport properties of the material, and therefore need to be carefully controlled in order to optimize its performance.

Despite its challenges, YBCO remains one of the most widely studied high-temperature superconductors due to its exceptional superconducting properties, as well as its ease of processing and stability. Ongoing research in this field continues to explore the fundamental physics of high-temperature superconductivity, as well as the potential applications of these materials in various technological fields.

2.2 Electrical Properties of $YBa_2Cu_3O_{7-\delta}$

The electrical properties of $YBa_2Cu3O7 - \delta$ (YBCO) are strongly influenced by its anisotropic crystal structure. In particular, the electrical transport properties are highly anisotropic, with much higher conductivity in the ab-plane than along the c-axis. This anisotropy is evident in the resistivity measurements, where the resistivity in the ab-plane is about two orders of magnitude smaller than that along the c-axis [51].

The anisotropy of the superconducting properties of YBCO is also pronounced. The superconducting transition temperature, T_c, is highest in the ab-plane and decreases as the temperature is lowered along the c-axis. The anisotropy of the London penetration depth, Λ_L, is also high, with Λ_L(ab) $\approx$ 200 nm and Λ_L(c) $\approx$ 1000 nm at 4 K [52]. The coherence length, ξ, is also highly anisotropic, with ξ(ab) $\approx$ 3 nm and ξ(c) $\approx$ 0.3 nm [53]. This anisotropy in Λ_L and ξ has important consequences for the behavior of YBCO in applied magnetic fields.

The anisotropy in the electrical and superconducting properties of YBCO is due to the crystal structure. The high conductivity in the ab-plane is a result of the CuO_2 planes, which are separated by non-conducting Y and Ba layers. The strong covalent bonding between the Cu and O atoms in the CuO_2 planes leads to the high conductivity in this direction. The low conductivity along the c-axis is due to the presence of the insulating Y and Ba layers.

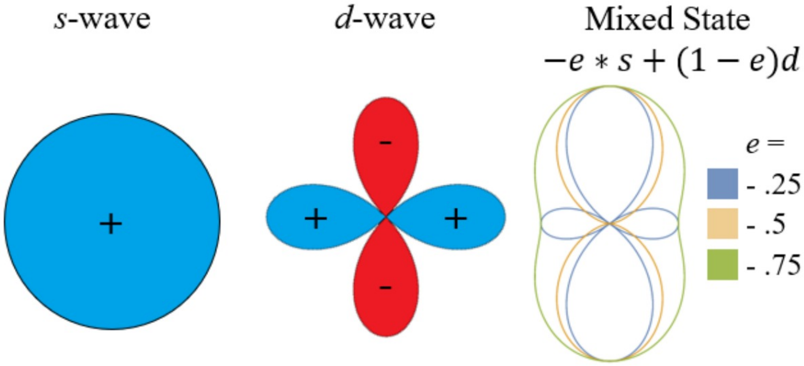

Figure 2.2: Visualization of the symmetries of states with s, d, and a mixture of s and d states, represented by the equation -e*s + (1 - e)d, for different values of e: 0.25, 0.5, and 0.75.

C$_{4v}$ Character Point Group				
Informal Name	Irreducible Representation	$R_{\pi/2}$	I_{axis}	Orbital Expression
s^+	A_{1g}	$+1$	$+1$	constant
s^-	A_{2g}	$+1$	-1	$xy(x^2 - y^2)$
$d_{x^2-y^2}$	B_{1g}	-1	$+1$	$x^2 - y^2$
d_{xy}	B_{2g}	-1	-1	xy

Table 2.1: Character point group of C_4v which reflects the symmetries of a planar square lattice

The anisotropy of the superconducting properties can be understood in terms of the anisotropy of the order parameter. In YBCO, the superconducting order parameter is believed to have a d-wave symmetry, which implies that it changes sign as the direction of the wave function changes as shown in Figure 2.2 and Table 2.1[50]. This leads to a nodal structure in the order parameter, where the magnitude of the order parameter is zero at certain points in momentum space. The nodal structure is more pronounced in the c-direction than in the ab-plane, leading to the strong anisotropy in the superconducting properties.

Overall, the anisotropic electrical and superconducting properties of YBCO make it a fascinating material for both fundamental and applied research. Understanding and controlling these anisotropic properties is important for the development of high-performance superconducting devices.

2.3 Multi-layer Devices

Multilayer devices are a class of superconducting devices that consist of multiple thin layers of superconducting materials separated by thin insulating layers. These devices have unique properties that arise from the interfaces between the superconducting and insulating layers, making them useful in a variety of applications[54].

One of the key advantages of multilayer devices is their ability to manipulate the superconducting properties of the constituent materials. For example, by adjusting the thickness of the superconducting layers, it is possible to modify the critical temperature, critical current density, and other important superconducting parameters. This can be useful in designing devices with specific performance characteristics for different applications[55].

Another advantage of multilayer devices is their ability to produce a variety of interesting and useful phenomena. For example, the interfaces between the superconducting and insulating layers can produce novel electronic states, such as Josephson junctions, which have important applications in quantum computing and sensing. Additionally, multilayer devices can exhibit interesting magnetic properties, such as magnetoresistance and flux trapping, which can be exploited in a range of magnetic sensing and imaging applications.

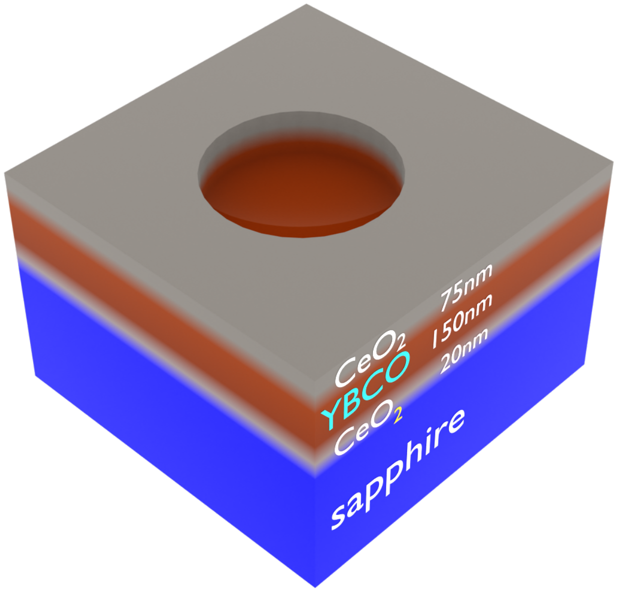

Figure 2.3: Multilayer VIA

Multilayer devices have found applications in a variety of fields, including magnetic resonance imaging (MRI), superconducting electronics, and quantum computing. In MRI, for example, superconducting multilayer devices are used to detect and measure magnetic fields in the human body with high precision and sensitivity. In superconducting electronics, multilayer devices are used to create complex circuits and signal processing systems. In quantum computing, multilayer devices are used to create and control qubits, the basic building blocks of quantum computers[56].

Overall, multilayer devices offer a powerful and versatile platform for exploring the properties of superconducting materials and designing new superconducting devices for a variety of applications.

Chapter 3

Design of YBCO Vias

The design of the experiment was focused on the fabrication of high-quality YBCO vias. Vias are small holes that penetrate through a material, and they are commonly used in electronic devices to create electrical connections between different layers. In the case of superconducting devices, vias are used to connect superconducting layers and create electrical pathways for current flow.

A multilayer structure was created at Ceraco GmbH using RCE process, which consisted of layers of YBCO and CeO_2 on r-plane sapphire. The YBCO layer at the bottom was intended to function as a ground plane and was given a thickness similar to that of the penetration depth of YBCO to ensure proper shielding. On the other hand, the thickness of the CeO_2 insulating layer was increased as much as possible to maximize its insulating properties and prevent cracking, which is a common issue in sapphire films, while keeping the total thickness of the heterostructure under 300 nm.

The multilayer heterostructures were deposited on five 2-inch r-plane sapphire wafers, which were placed in the center of the deposition plate. To prevent lattice mismatches with the substrate, a 20-nm thick buffer layer of CeO_2 was first grown, followed by a 150-nm thick YBCO film as the bottom ground plane. The copper content was reduced to ensure smooth films and prevent pinhole shorts through subsequent layers, which resulted in a reduced T_C and J_C. Next, a 75-nm thick CeO_2 layer was deposited, and the TC and JC of the bottom YBCO layer were measured to be 83.6 K and 1.0 MA/cm2, respectively, using an inductive Cryoscan.

The YBCO vias were designed to have a diameter in the range of 100 microns to 2 microns and a height of 100 nanometers. These dimensions were chosen based on the desired electrical properties of the device and the capabilities of the fabrication equipment. The vias were designed to be spaced 50 microns apart in a square lattice pattern.

To achieve this, the experiment involved the use of photolithography and ion milling techniques to create vias in the CeO_2-YBCO films. The process involved the deposition of a resist layer on top of the CeO_2 film, which was then exposed to a pattern of UV light. The unexposed resist was then developed away, leaving a pattern of resist that protected the YBCO film underneath. 75nm CeO_2 and 45nm bottom YBCO film was then ion milled to remove the exposed areas and create the desired via pattern.

The design of the experiment involved a number of key decisions and considerations. One of the primary concerns was the potential for damage to the YBCO film during the ion milling process. This required careful optimization of the ion milling parameters, including the ion energy and ion beam angle, to minimize damage to the YBCO film.

Another important consideration was the size and shape of the vias. The size of the vias was critical to achieving the desired level of integration, as smaller vias allowed for closer spacing of components and higher packing densities. The shape of the vias was also important, as the desired shape would depend on the specific application and the materials being integrated.

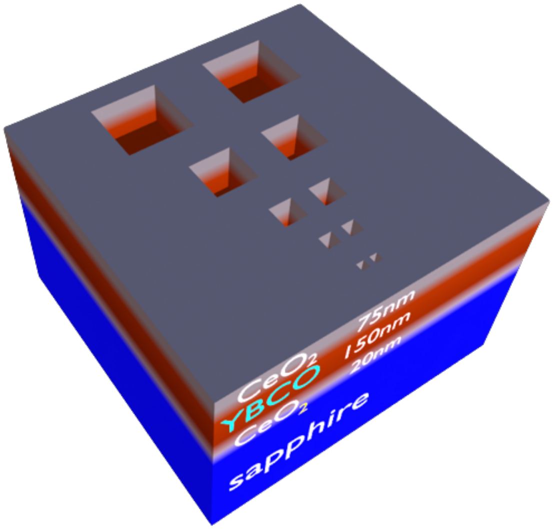

Figure 3.1: The diagram shows the structure of a multilayer film composed of a 20-nm CeO_2 buffer layer, 150-nm YBCO layer at the bottom serving as a ground plane, 75-nm CeO_2 insulating layer on a sapphire substrate

.

The sapphire wafers with a bottom 150-nm YBCO layer and a 75-nm CeO_2 layer were taken back to the vacuum chamber for a second deposition. An additional CeO_2 buffered sapphire substrate was also included. A 35-nm YBCO layer was grown on top of the previous layers, followed by a 200-nm gold contact layer as show in Figure 3.1. To improve the electrical properties, the copper content was increased for this deposition. The second 35-nm YBCO layer was measured to have a T_c of 84.8 K and a J_C of 2.3 MA/cm2 using a cryoscan of the extra test substrate. The whole stack of thin films (150 nm YBCO/75 nm CeO_2/35 nm YBCO) was measured to have a J_C of around 1.2 MA/cm2 in a third cryoscan. The current density of the entire structure with the two YBCO layers was estimated to be 1.25 MA/cm2, which is consistent with the measured value of 1.2 MA/cm2. This suggests that the quality of the 35-nm YBCO layer on top of the CeO_2/YBCO layers is similar to the YBCO film on the test substrate.

Overall, the design of the YBCO vias experiment involved a careful balance of competing factors, including the need to create vias that were small and precise, while also minimizing damage to the YBCO film. By carefully considering these factors and optimizing the process, we were able to successfully create superconducting vias in YBCO films, opening up new possibilities for integrating these films with other materials and components.

Chapter 4

Structural Characterization

4.1 Optical Microscope

The optical microscope is a valuable tool used for the characterization of vias after the argon ion milling process. It allows for the visual inspection of the surface morphology and topography of the vias, providing important insights into their structural properties.

In our study, we specifically examined the vias that underwent ion milling at different stage angles, namely 45 degrees and 30 degrees. Through the optical microscope, we observed distinct differences between the two.

For the vias that underwent ion milling at a 45-degree stage angle, we observed a clean and uniform surface without any noticeable redeposition. This suggests that the ion milling process at this angle effectively removed material without causing significant redeposition, resulting in a smoother surface.

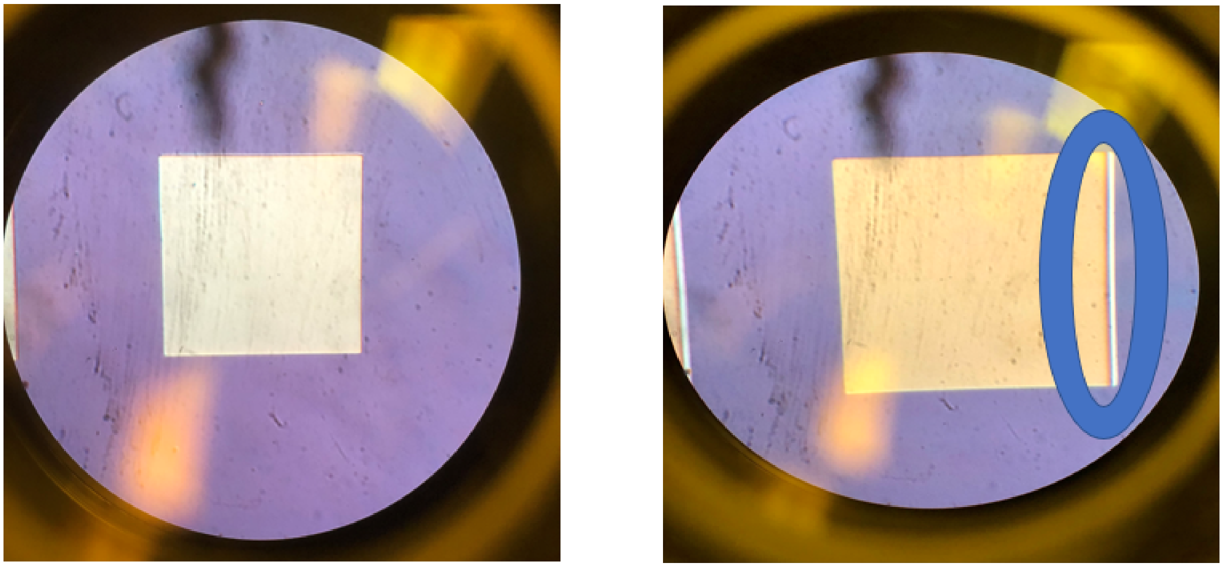

Figure 4.1: Optical image of 100 micron via at 45 degree (left), 30 degree (right) stage ion milled with notable redeposition on the edge (blue circle).

On the other hand, the vias that were ion milled at a 30-degree stage angle exhibited redeposition of material on the surface. This redeposition led to the formation of non-uniform features and roughness, which can impact the overall quality and functionality of the vias.

By utilizing the optical microscope, we were able to visually compare and assess the surface characteristics of the vias, highlighting the importance of the ion milling stage angle in minimizing redeposition and achieving a smoother surface for optimal performance.

4.2 Atomic Force Microscopy (AFM)

In order to investigate the structural properties of the samples, atomic force microscopy (AFM) was performed. AFM is a powerful tool for imaging surfaces with high resolution and sensitivity to topography.

Below present the AFM data for the four different micron sizes (25, 10, 4, and 2) and compare the results for each angle (45°, 30°, 20°, and 15°) of ion milling. It will also discuss any trends or differences observed in the AFM images.

4.2.1 25 Micron Size

This subsection will present the AFM data for the 25 micron size and compare the results for each angle of ion milling.

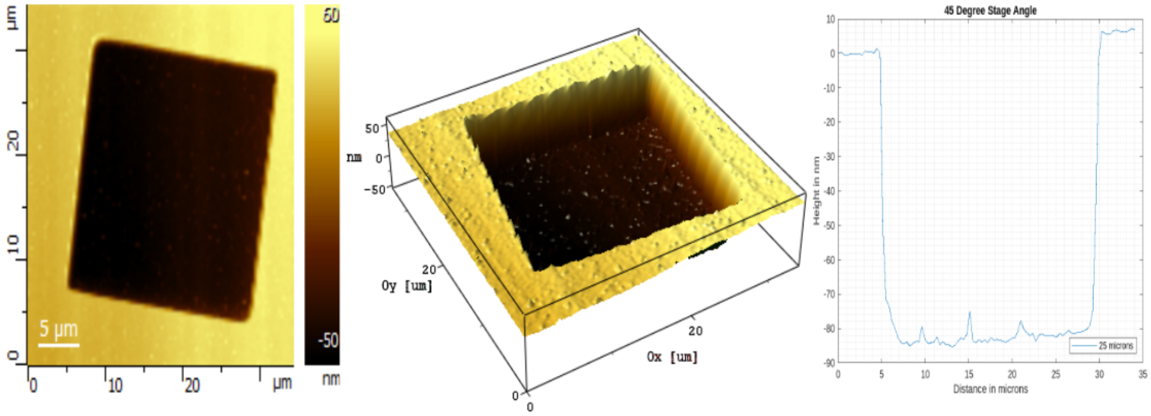

Figure 4.2: 25 Micron VIA at 45° stage angle.

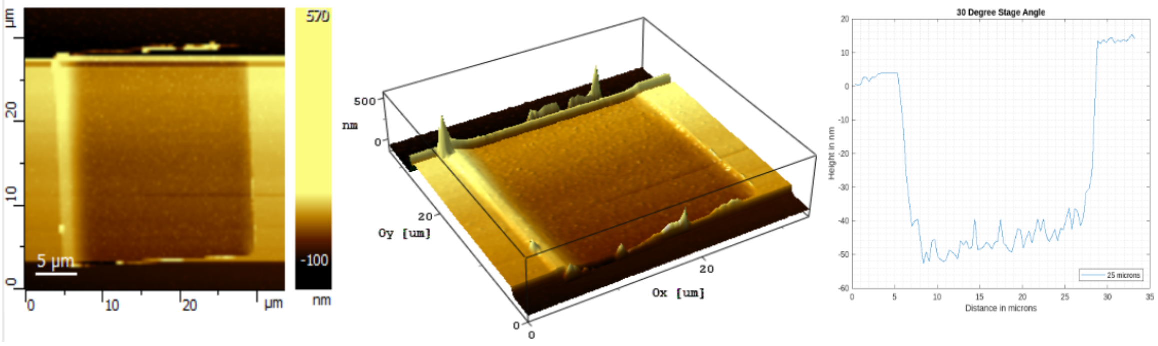

Figure 4.3: 25 Micron VIA at 30° stage angle.

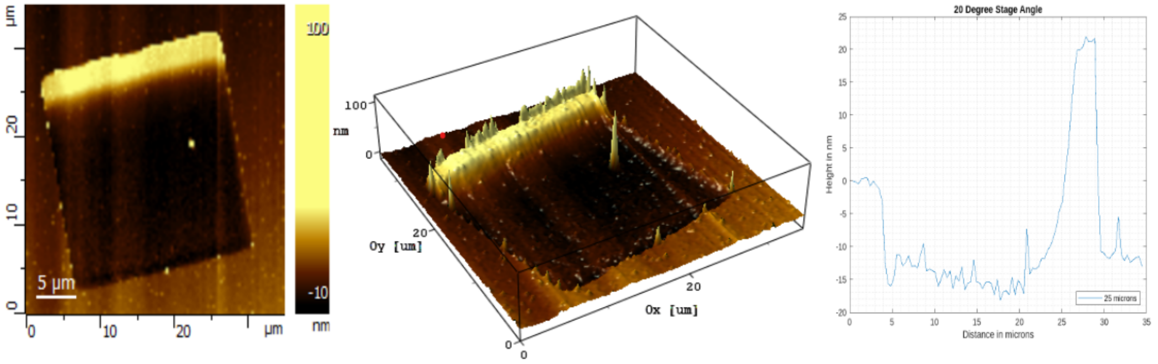

Figure 4.4: 25 Micron VIA at 20° stage angle.

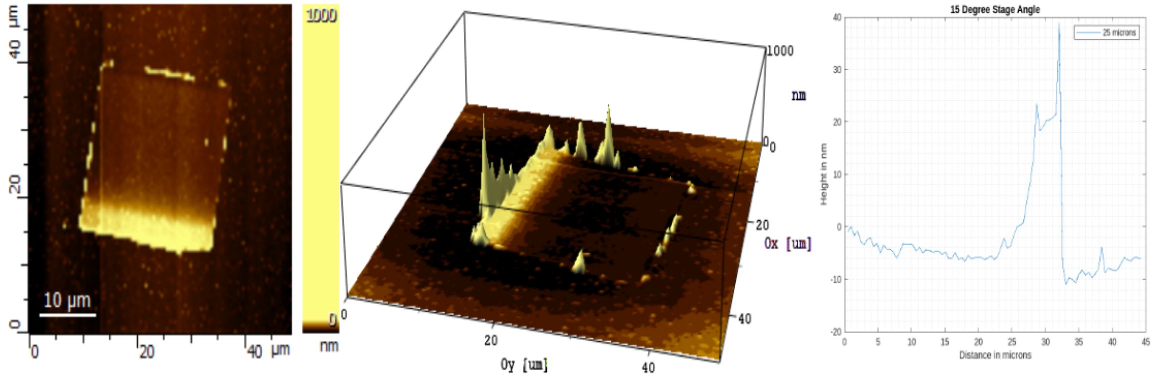

Figure 4.5: 25 Micron VIA at 15° stage angle.

4.2.2 10 Micron Size

This subsection will present the AFM data for the 10 micron size and compare the results for each angle of ion milling.

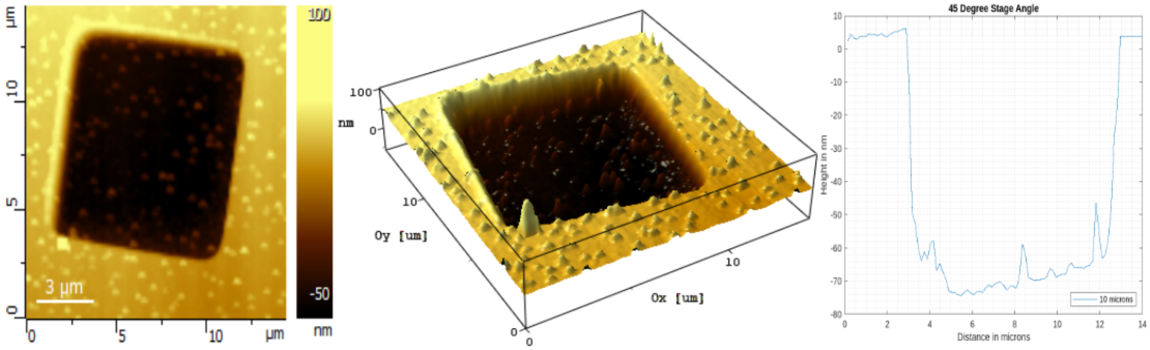

Figure 4.6: 10 Micron VIA at 45° stage angle.

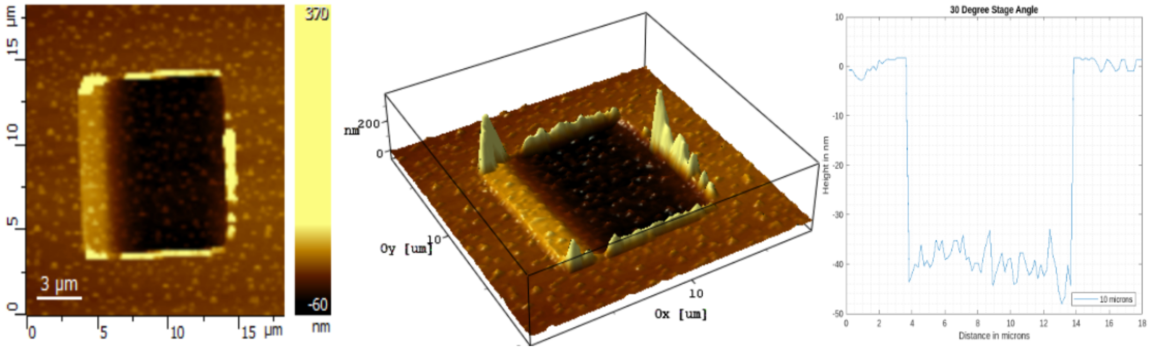

Figure 4.7: 10 Micron VIA at 30° stage angle.

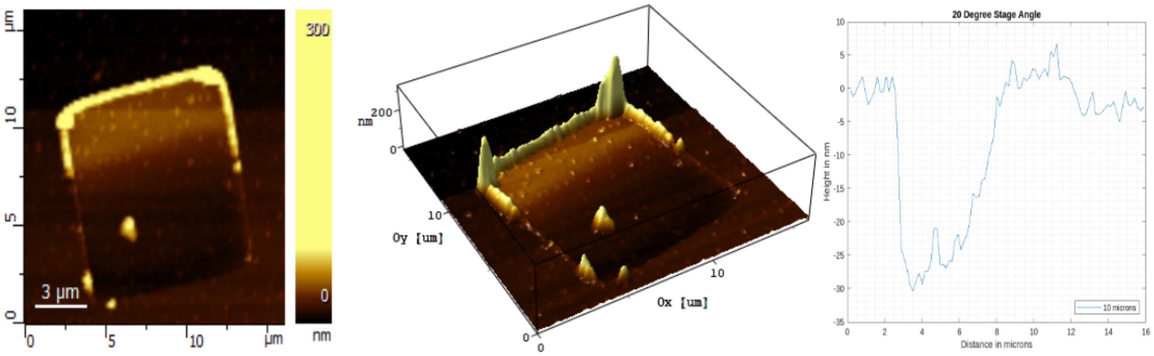

Figure 4.8: 10 Micron VIA at 20° stage angle.

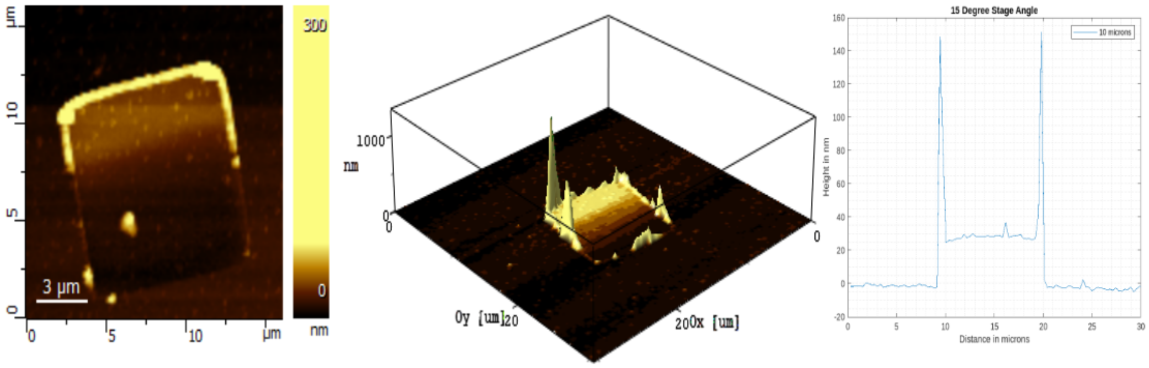

Figure 4.9: 10 Micron VIA at 15° stage angle.

4.2.3 4 Micron Size

This subsection will present the AFM data for the 4 micron size and compare the results for each angle of ion milling.

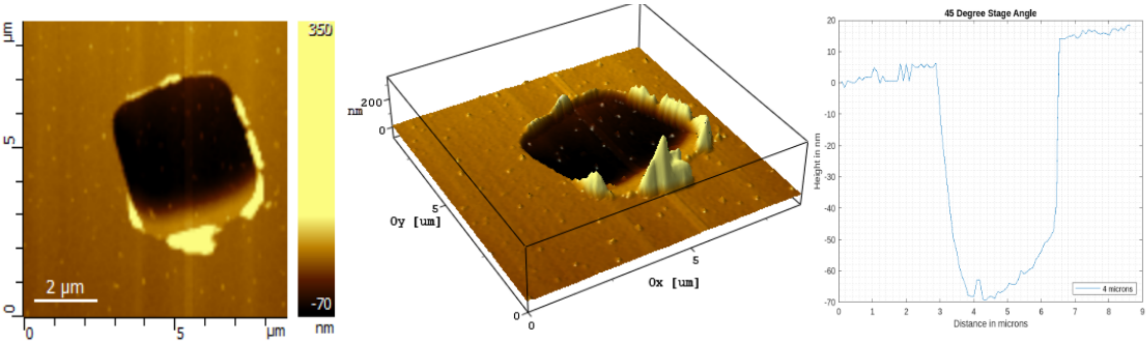

Figure 4.10: 4 Micron VIA at 45° stage angle.

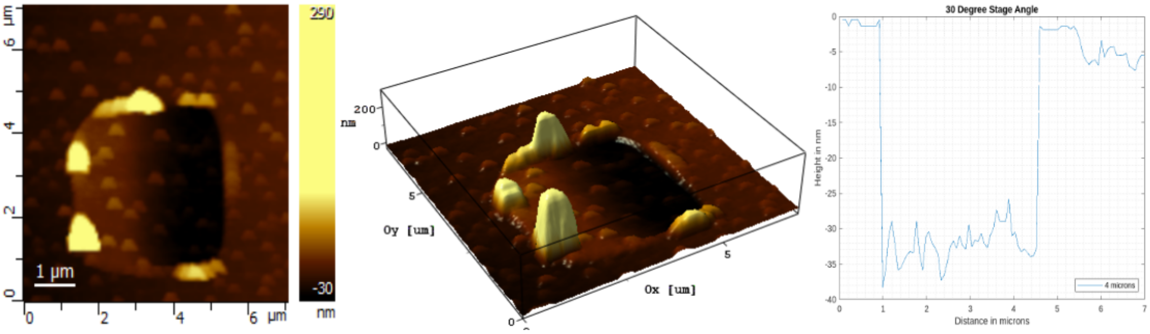

Figure 4.11: 4 Micron VIA at 30° stage angle.

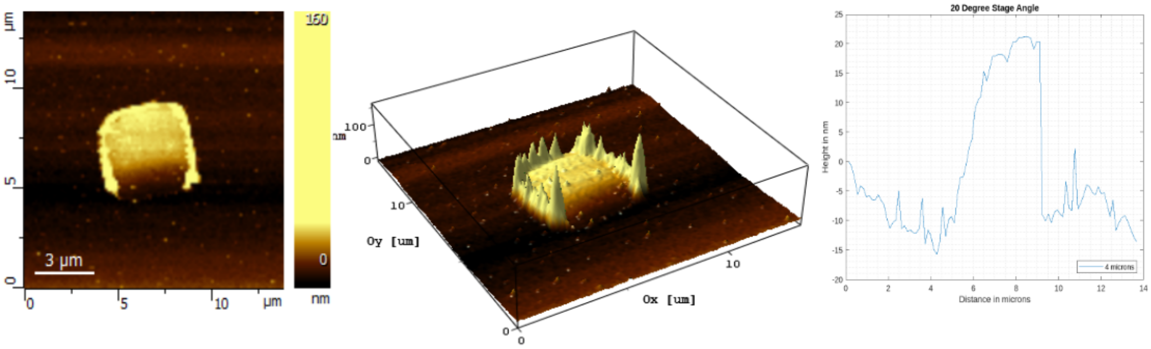

Figure 4.12: 4 Micron VIA at 20° stage angle.

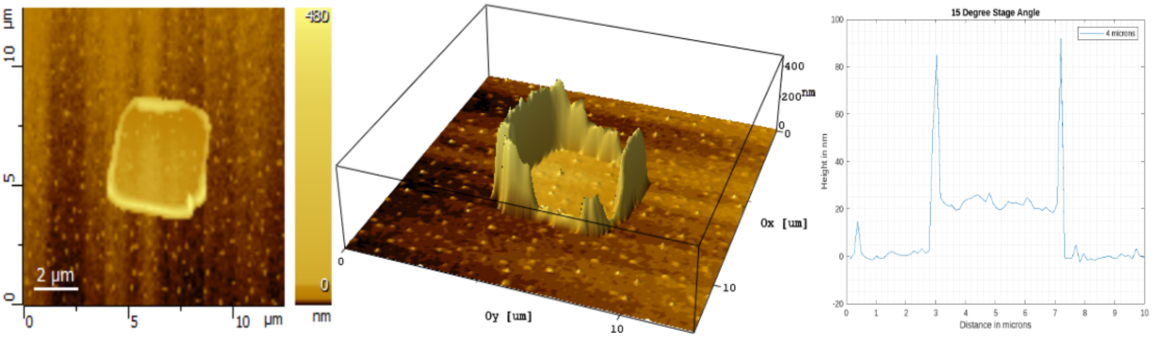

Figure 4.13: 4 Micron VIA at 15° stage angle.

4.2.4 2 Micron Size

This subsection will present the AFM data for the 2 micron size and compare the results for each angle of ion milling.

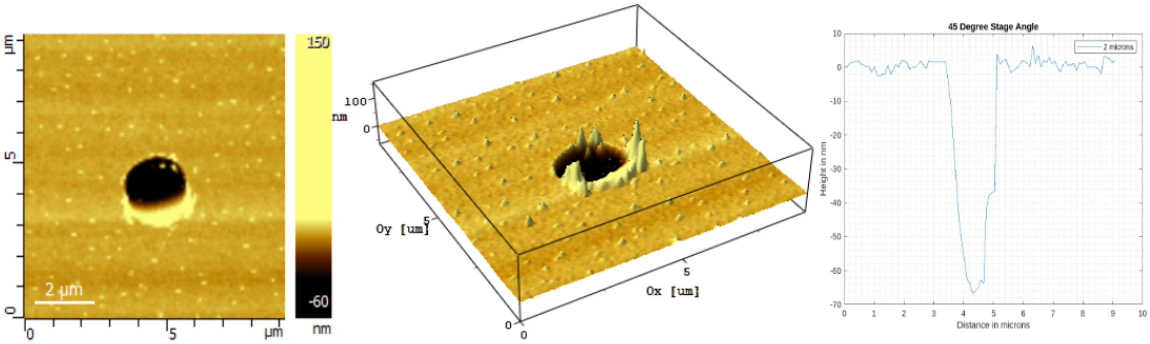

Figure 4.14: 2 Micron VIA at 45° stage angle.

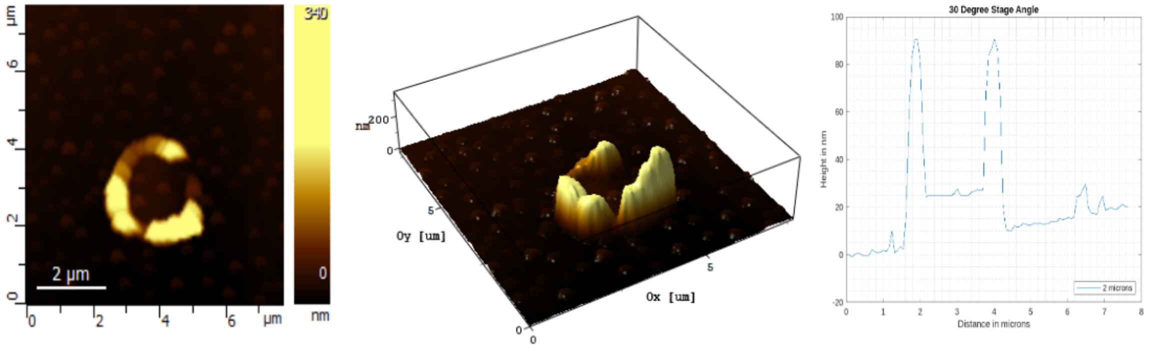

Figure 4.15: 2 Micron VIA at 30° stage angle.

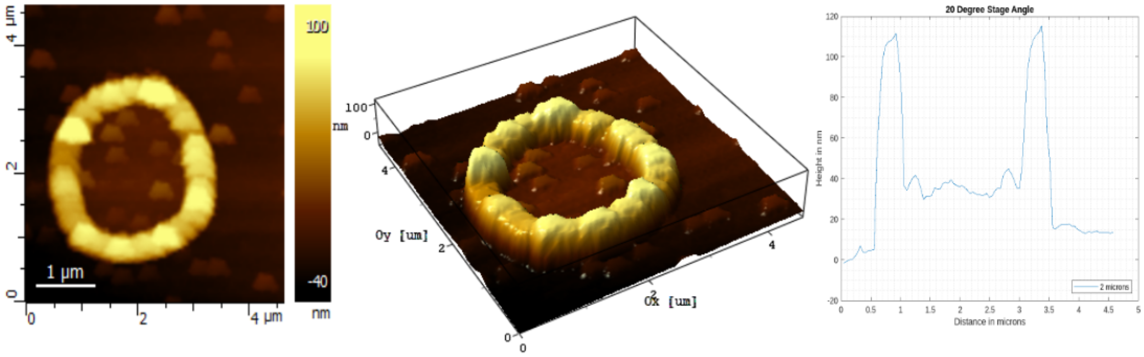

Figure 4.16: 2 Micron VIA at 20° stage angle.

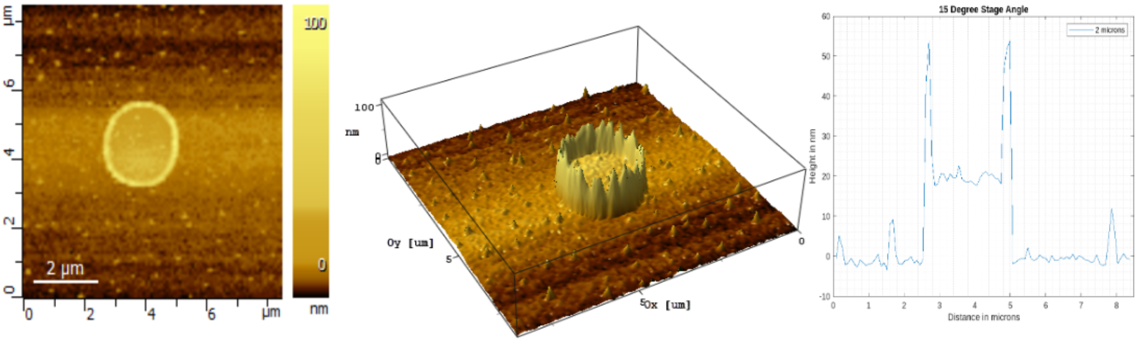

Figure 4.17: 2 Micron VIA at 15° stage angle.

The AFM data revealed important information about the surface morphology and roughness of the samples. Analysis of the data showed that the 45 degree angle ion milling was the most effective in producing a smooth and uniform surface compared to other angles tested, including 30 degrees, 20 degrees, and 15 degrees.

Further analysis of the AFM data provided insight into the crystal structure of the samples. Peaks in the AFM images indicated the presence of crystalline domains, while valleys represented areas of amorphous or disordered material. By measuring the size and distribution of these domains, we were able to determine important structural parameters such as grain size and orientation.

As the size and ion milling stage angle of the vias changed, it introduced variations in the surface morphology and crystal structure of the samples. The AFM data revealed that smaller size of the vias led to a higher likelihood of surface roughness and non-uniformity. This can be attributed to the smaller area being subjected to ion milling, resulting in a greater chance of material redeposition and surface irregularities.

Similarly, altering the ion milling stage angle from the optimal 45 degrees to angles such as 30 degrees, 20 degrees, and 15 degrees resulted in noticeable changes in the surface characteristics. These variations included increased surface roughness, uneven milling patterns.

Overall, the AFM data provided valuable information about the structural properties of the samples, helping to guide further analysis and interpretation of the results.

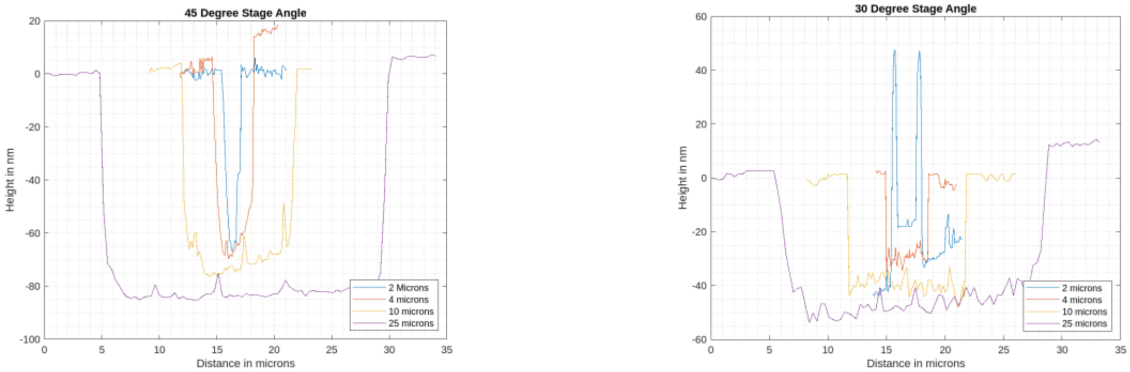

(a) AFM data showing the surface morphology of VIAs at a 45° angle of ion milling.

(b) AFM data showing the surface morphology of VIAs at a 30° angle of ion milling.

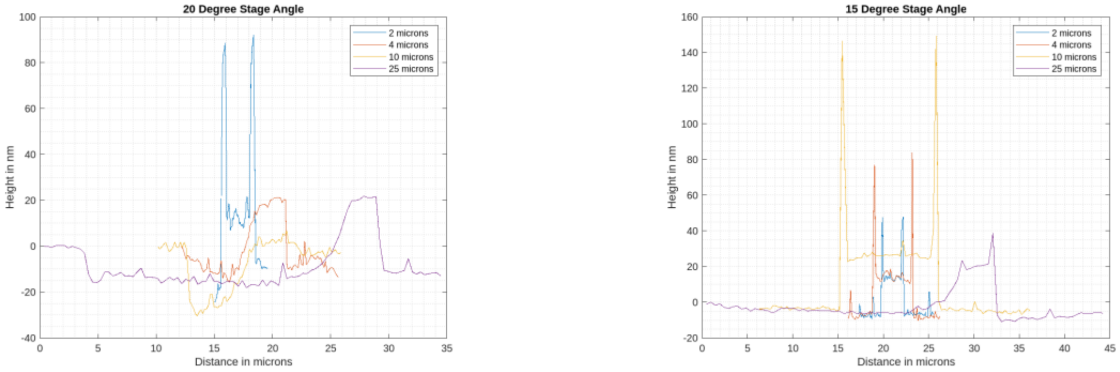

(c) AFM data showing the surface morphology of VIAs at a 20° angle of ion milling.

(d) AFM data showing the surface morphology of VIAs at a 15° angle of ion milling.

Figure 4.18: AFM images of VIAs of different micron sizes (25, 10, 4, and 2) after ion milling at four different angles (45°, 30°, 20°, and 15°).

4.3 OXY-Plasma Asher

The oxy plasma asher is a technique used to remove organic material from the surface of a sample, including redeposited material that may result from the ion milling process. In our study, we hypothesized that the redeposition observed in the vias, particularly those ion milled at a 30-degree, 20-degree and 15 degree stage angle, might be attributed to the hardened photo resist.

To investigate this, we employed the oxy plasma asher as a potential solution. We conducted a series of experiments using different durations of oxy plasma asher treatment, starting with 10 seconds and then extending to an additional 1 minute and an additional 10 minutes.

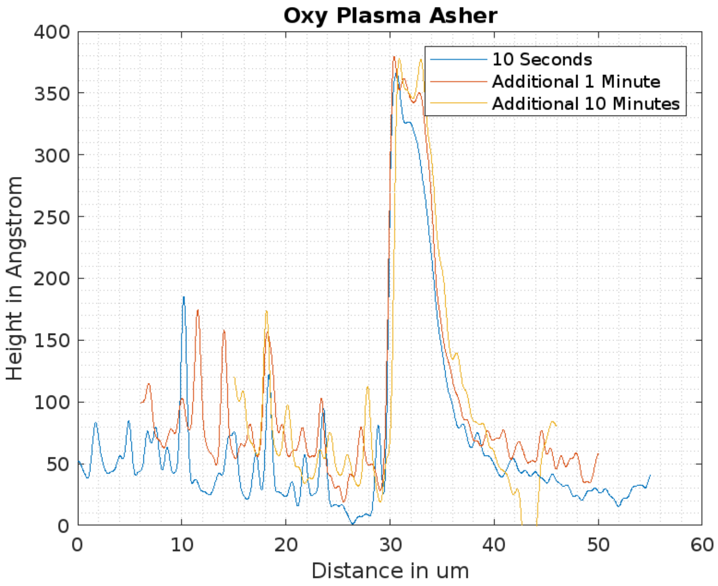

Figure 4.19: OXY-Plasma ashing on redeposited edges of the VIAs

Surprisingly, despite the variations in treatment time, we did not observe any significant change in the redeposition of material. This finding led us to conclude that our initial assumption, which attributed the redeposition to the hardened photoresist, was incorrect.

The oxy plasma asher treatment did not have the desired effect of removing or reducing the redeposition, suggesting that the source of redeposition might be more complex than anticipated. Further investigation is needed to identify the underlying factors contributing to the redeposition and to develop alternative strategies for mitigating this issue.

In summary, our attempts to address the redeposition issue using oxy plasma asher treatment did not yield the expected results. This finding highlights the need for additional research to uncover the root cause of the redeposition and explore alternative methods for achieving a cleaner and more uniform surface in the fabrication of vias for superconducting devices.

4.4 Scanning Electron Microscopy (SEM) - Energy dispersive X-ray (EDX) analysis

To gain further insights into the redeposited material in the vias, we employed scanning electron microscopy with energy-dispersive X-ray spectroscopy (SEM-EDX) imaging. This technique allowed us to analyze the elemental composition of the samples and identify the source of the redeposited material.

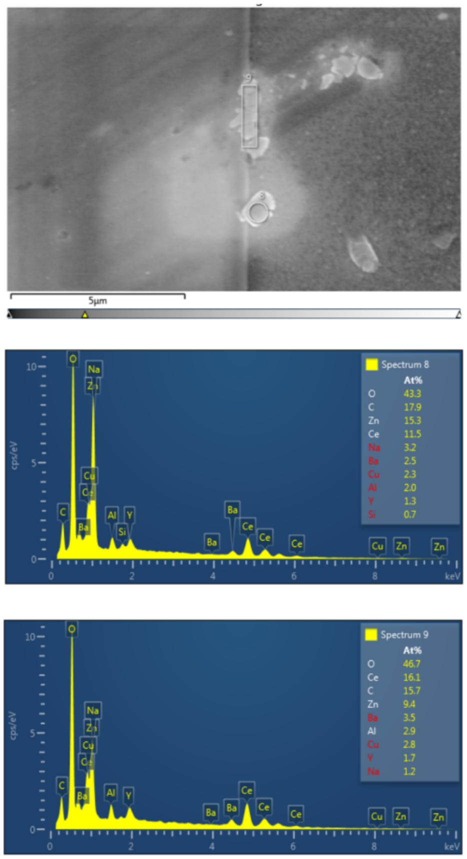

Spectrum 8

	At%
O	43.3
C	17.9
Zn	15.3
Ce	11.5
Na	3.2
Ba	2.5
Cu	2.3
Al	2.0
Y	1.3
Si	0.7

Spectrum 9

	At%
O	46.7
Ce	16.1
C	15.7
Zn	9.4
Ba	3.5
Al	2.9
Cu	2.8
Y	1.7
Na	1.2

Figure 4.20: SEM-EDX mapping of redeposited material on the VIAs

During the SEM-EDX imaging, we observed the presence of copper contaminants in the vias. By examining the distribution and concentration of copper using the EDX analysis, we were able to trace back the origin of these contaminants. The results indicated that the copper contamination originated from the ion milling stage itself.

The SEM-EDX imaging provided valuable information about the nature of the redeposited material and confirmed that it was indeed copper. This finding was crucial in understanding the root cause of the redeposition issue and guiding subsequent steps to address it.

Based on the SEM-EDX results, we concluded that the redeposition of material in the vias was primarily attributed to the copper present on the ion milling stage. This discovery highlighted the importance of thorough cleaning and maintenance of the ion milling equipment to minimize copper contamination and ensure the production of high-quality vias.

The application of SEM-EDX imaging to the vias provided valuable insights into the presence of redeposited material. Through the analysis, we were able to identify the source of the redeposition issue. The results indicated that the redeposited material in the vias was primarily attributed to copper contamination originating from the ion milling stage.

Chapter 5

Discussion of Results

The discussion of results is a critical part of any research study as it allows for the interpretation and analysis of the data collected. In this chapter, we will correlate the structural properties of the samples and analyze what worked and what did not work.

The structural characterization results showed that the 45-degree angle ion milling was the most effective in producing a smooth and uniform surface compared to other angles tested. This smooth surface was crucial for the growth of the top YBCO layer. The AFM data also provided important information about the crystal structure, including grain size and orientation.

Unfortunately, we do not have any electrical characterization results for this study as the samples were sent to Crystal Grower Ceraco in Germany for the growth of the top YBCO layer. However, we can predict that the smooth and uniform surface produced by the 45-degree angle ion milling will lead to better electrical properties in the final samples.

In terms of what did not work, we encountered some challenges during the ion milling process at angles other than 45 degrees. The surfaces produced by these angles were rough and non-uniform, making it difficult to grow a high-quality YBCO layer. It is possible that the failure in these cases was due to the lack of control over the ion beam direction, leading to a non-uniform milling pattern.

In conclusion, the structural characterization results provide valuable insights into the effect of ion milling angle on the surface morphology and crystal structure of the samples. The smooth and uniform surface produced by the 45-degree angle ion milling is likely to lead to better electrical properties in the final samples. However, further electrical characterization is needed to confirm this hypothesis. The challenges encountered during ion milling at angles other than 45 degrees highlight the importance of careful process optimization and control to achieve high-quality samples.

Chapter 6

Conclusions

In conclusion, our work has significant implications for the field of HTS electronics. By utilizing commercial YBCO films with CeO as an insulator on giant sapphire wafers, we have developed a process that is scalable for large area circuits like SC digital. This is a major breakthrough as all prior vias could only be on small substrates and used PLD. Our results have shown that the 45 degree angle ion milling is the most effective in producing a smooth and uniform surface. Additionally, the AFM data provided important insights into the crystal structure of the samples, which can inform future research in the field.

Although we do not yet have results for the electrical characterization of the vias, we believe that our process has the potential to significantly improve the performance of HTS electronics. The use of commercial YBCO films with CeO as an insulator on giant sapphire wafers can lead to the development of high-performance large area circuits, which can have a wide range of applications in areas such as medical imaging, energy storage, and quantum computing.

Overall, our work has introduced a new process using different materials that can significantly impact the field of HTS electronics. We are confident that our findings will inspire further research in this area and lead to the development of even more advanced technologies in the future.

Bibliography

[1] Heike Kamerlingh Onnes. Further experiments with liquid helium. c. on the resistance of pure mercury at helium temperatures. d. on the disappearance of the resistance of mercury. *Communications from the Physical Laboratory at the University of Leiden*, 1911:121–128, 1911.

[2] Michael Tinkham. *Introduction to Superconductivity.* Dover Publications, 1996.

[3] Brian D. Josephson. Possible new effects in superconductive tunnelling. *Physical Review Letters*, 1:251–253, 1962.

[4] J. Bardeen, L. N. Cooper, and J. R. Schrieffer. Theory of superconductivity. *Physical Review*, 108(5):1175–1204, 1957.

[5] V. L. Ginzburg and L. D. Landau. On the theory of superconductivity. *Zhurnal eksperimental'noi i teoreticheskoi fiziki*, 20:1064–1082, 1950.

[6] P. W. Anderson. Plasmons, gauge invariance, and mass. *Physical Review*, 130(1):439–442, 1963.

[7] J. G. Bednorz and K. A. Müller. Possible high-tc superconductivity in the ba-la-cu-o system. *Zeitschrift für Physik B Condensed Matter*, 64(2):189–193, 1986.

[8] Leon N Cooper. Bound electron pairs in a degenerate fermi gas. *Physical Review*, 104(4):1189, 1956.

[9] Daniel C Mattis. *The theory of magnetism I: Statics and dynamics.* Springer Science & Business Media, 1993.

[10] Pierre-Gilles DeGennes. *Superconductivity of Metals and Alloys.* Benjamin, 1966.

[11] Claude Cohen-Tannoudji, Bernard Diu, and Franck Laloë. *Quantum mechanics*, volume 2. Wiley, 1977.

[12] J. Schmalian, Peter G. Wolynes, and Steven A. Kivelson. Colloquium: Superconductivity and superfluidity. *Reviews of Modern Physics*, 70(3):1033–1047, 1998.

[13] Alexander Altland and Ben Simons. *Condensed matter field theory*. Cambridge University Press, 2010.

[14] Charles Kittel. *Introduction to Solid State Physics*. Wiley, 8 edition, 2004.

[15] BCS Theory. In *Encyclopædia Britannica*. 2022.

[16] D. J. Scalapino. The superconducting state. *Physics Reports*, 3(4):179–310, 1969.

[17] W. L. McMillan. Transition temperature of strong-coupled superconductors. *Physical Review*, 167(2):331–344, 1968.

[18] P W Anderson. Theory of dirty superconductors. *Journal of Physics and Chemistry of Solids*, 11(1-2):26–30, 1959.

[19] P. J. Hirschfeld and N. Goldenfeld. Effect of scattering on density of states and pairing in superconductors. *Physical Review B*, 48(7):4219–4238, 1993.

[20] H. Suhl. Effects of impurities on superconducting metals. *Physical Review Letters*, 3(11):552–554, 1959.

[21] A. I. Rusinov. Effect of scattering on the energy spectrum of superconductors. *Soviet Journal of Experimental and Theoretical Physics*, 29:1101–1106, 1969.

[22] S. M. Sze. *Physics of semiconductor devices*. Wiley, 2 edition, 1981.

[23] L. Esaki. New phenomenon in narrow germanium p-n junctions. *Physical Review Letters*, 33(8):495–497, 1974.

[24] J. G. Simmons. Generalized formula for the electric tunnel effect between similar electrodes separated by a thin insulating film. *Journal of Applied Physics*, 34(6):1793–1803, 1963.

[25] Lev P Pitaevskii and Sandro Stringari. *Bose-Einstein Condensation*. Number 116. Oxford University Press, 2003.

[26] C. J. Pethick and H. Smith. *Bose-Einstein condensation in dilute gases*. Cambridge University Press, 2002.

[27] Franco Dalfovo, Stefano Giorgini, Lev P Pitaevskii, and Sandro Stringari. Theory of bose-einstein condensation in trapped gases. *Reviews of Modern Physics*, 71(3):463–512, 1999.

[28] M. H. Anderson, J. R. Ensher, M. R. Matthews, C. E. Wieman, and E. A. Cornell. Observation of bose-einstein condensation in a dilute atomic vapor. *Science*, 269(5221):198–201, 1995.

[29] Konstantin K Likharev. *Single-electronics and beyond: Advances in electronics and electron physics*, volume 181. Academic Press, 2015.

[30] Göran Wendin and Vitaly Shumeiko. Superconducting qubits. In *Handbook of Theoretical and Computational Nanotechnology*, volume 3, pages 321–386. American Scientific Publishers, 2007.

[31] Michel H Devoret and Robert J Schoelkopf. Superconducting circuits for quantum information: An outlook. *Science*, 339(6124):1169–1174, 2013.

[32] John Clarke and Alexei I Braginski. *The SQUID handbook: Fundamentals and technology of SQUIDs and SQUID systems.* Wiley, 2004.

[33] I. Giaever. Electron tunneling between two superconductors. *Physical Review Letters*, 5(3):147–148, 1960.

[34] P. Fulde. Superconductivity in alloys and impurity systems. *Adv. Phys.*, 18(2):191–242, 1969.

[35] R H Koch, DJ van Harlingen, and J Clarke. Fiske modes in josephson-junction qubits. *Physical Review B*, 76(18):184522, 2007.

[36] RL Kautz and S Sridhar. Theory of the fiske effect in superconducting thin films. *Physical Review B*, 48(8):5322, 1993.

[37] ME Tobar. *Microwave superconductivity*, volume 38. Springer Science Business Media, 2006.

[38] FC Wellstood, C Urbina, and J Clarke. Fiske steps and the measurement of the electron charge. *Applied Physics Letters*, 65(26):3444–3446, 1994.

[39] T. Van Duzer and C.W. Turner. *Principles of Superconductive Devices and Circuits.* Elsevier Science, 1999.

[40] A.V. Ustinov and C. Russo. *Nonlinear Dynamics of Josephson Junctions and Superconducting Devices.* Springer Science & Business Media, 2012.

[41] G. Wendin. Quantum information processing with superconducting circuits: a review. *Reports on Progress in Physics*, 80(10):106001, 2017.

[42] J.E. Mooij and Yu.V. Nazarov. Superconducting nanowires as quantum phase-slip junctions. *Nature Physics*, 2:169–172, 2006.

[43] D A Dahl and J E Lukens. Linear arrays of josephson junctions. *IEEE Transactions on Magnetics*, 23:1186–1189, 1987.

[44] S E Russek and D O Klyshko. Superconducting quantum interference filters. *Proceedings of the IEEE*, 92:1597–1612, 2004.

[45] J H Judy. Josephson-junction arrays for metrology. *Journal of Research of the National Institute of Standards and Technology*, 97:215–230, 1992.

[46] P. A. Lee, N. Nagaosa, and X.-G. Wen. Doping a mott insulator: Physics of high-temperature superconductivity. *Reviews of Modern Physics*, 78(1):17–85, 2006.

[47] J. Schmalian, D. Pekker, and C. S. Ting. Superconductivity: The dark matter of quantum materials. *Nature Physics*, 15(11):1051–1057, 2019.

[48] V. L. Ginzburg. Superconductivity and superfluidity (what i have and have not managed to do). *Physics-Uspekhi*, 48(12):1235–1246, 2005.

[49] D. Daghero, R. S. Gonnelli, and G. A. Ummarino. High-temperature superconductivity: An overview. *Superconductor Science and Technology*, 23(3):33001–33029, 2010.

[50] Jay Clayton Lefebvre and Shane A. Cybart. *Cuprate Superconductivity Analysis via Helium Ion Microscopy.* PhD thesis, University of California, Riverside, 2021. Dissertations & Theses @ University of California; ProQuest Dissertations & Theses A&I.

[51] Hidenori Takagi and Shin-ichi Uchida. Superconductivity in cu-o compounds. *Physical Review B*, 43(5):3872, 1991.

[52] C Panagopoulos, T Xiang, JR Cooper, and YQ Wang. Anisotropic superconducting properties of yba2cu3o7- single crystals. *Physical Review B*, 61(6):3808, 2000.

[53] J Mosqueira, Y Fasano, C Carballeira, D Pavuna, J Veira, and F Soto. Anisotropy of the coherence length in yba2cu3o7 single crystals. *Physical Review B*, 58(1):295, 1998.

[54] John M L Warman. Superconducting multilayer structures. *Reports on Progress in Physics*, 59(9):925–986, 1996.

[55] Judith L MacManus-Driscoll. Superconductor/ferromagnet multilayer structures. *Journal of Materials Science*, 42(4):1037–1055, 2007.

[56] Chang-Beom Eom and Jean-Marc Triscone. Multilayer superconducting thin films: artificial lattices and superlattices. *Journal of Physics: Condensed Matter*, 16(1):R25–R44, 2004.

[57] J. R. Schrieffer. *Theory of Superconductivity*, volume 22. CRC press, 1964.

[58] James F. Annett. *Superconductivity, superfluids, and condensates.* Oxford University Press, 2004.

[59] Wolfgang Ketterle. Bose–einstein condensation in gases. *Advances in Atomic, Molecular, and Optical Physics*, 37:181–236, 1996.

[60] R J Schoelkopf and S M Girvin. Wiring up quantum systems. *Nature*, 451:664–669, 2008.

[61] J. F. Annett. *Superconductivity, Superfluids, and Condensates.* Oxford University Press, 2004.

[62] Supratim Sengupta and Subash Pai. Multilayered superconductors: a review. *Journal of Materials Science*, 43(17):5583–5603, 2008.

[63] Yan-Ting Wang and Shane Cybart. *Tunneling Studies of Superconducting Cuprate with Helium Disordered Barriers*. PhD thesis, University of California, Riverside, 2021. Dissertations Theses @ University of California; ProQuest Dissertations Theses AI, Database copyright ProQuest LLC;.

[64] Z Chen, J Wang, L Wang, W Liu, Y Yao, and X Liao. Progress in high-T_c superconductors: materials and applications. *Journal of Physics D: Applied Physics*, 55(10):103001, 2022.

[65] X Zhang, X Zhao, S Zhang, H Zhou, H Huang, Y Zhu, Y Zheng, J Xu, and X Sun. High-T_c superconducting microwave electronics. *Science China Physics, Mechanics & Astronomy*, 64(9):209504, 2021.

[66] Qiang Li, Xiaoping Wu, KK Wong, and HT Wong. Microwave dielectric properties of superconducting yba2cu3o7- thin films. *Applied physics letters*, 58(22):2515–2517, 1991.

[67] Alexis P Malozemoff and Michael P Fisher. Superconductivity and magnetic fields. *Physics today*, 41(2):57–63, 1988.

[68] Bernd T Matthias, John K Hulm, Eugene Corenzwit, Theodore H Geballe, CB Geller, GL Hull, JC Jamieson, M Munchmeyer, and K Takano. Superconductivity in alloys of be with cu, ag, and au. *Physical Review*, 109(2):604–605, 1958.

[69] PU Sastry, BS Bhatia, VV Kulkarni, G Ravikumar, R Gopalakrishnan, and SM Bhagat. Properties and potential of yba2cu3o7- superconductor films. *Bulletin of materials science*, 19(1):93–102, 1996.